Chapter 8

CONSTANT STRESS AND PRESSURE RHEOLOGY OF COLLOIDAL SUSPENSIONS: THE EFFECTS OF HYDRODYNAMIC INTERACTIONS

8.1 Introduction

Dense colloidal suspensions are widely present in nature and in industry [1–3]. Their rich rheological behaviors, including yielding [4–6], shear thinning [7–9], and shear thickening [10, 11], lead to phenomena such as flow instability [12] and particle migration [13, 14]. These behaviors arise from the complex interplay among Brownian motion, hydrodynamic interactions (HIs), and interparticle forces at high particle concentrations. To develop novel materials and applications based on dense colloidal suspensions, a quantitative understanding of their structure, dynamics, and rheology is necessary.

An essential feature of dense colloidal suspensions is the emergence of solid-like behaviors, which is commonly found in amorphous materials including metallic glasses, granular matter, and polymer melts, with increasing density, decreasing temperature, or reducing imposed stress. The flow-arrest transitions of amorphous materials are succinctly summarized by the "jamming diagram", suggesting that the system behaviors are governed by a special point J in the zero-temperature, zero-inverse-density, and zero-stress limit [15–17]. In hard-sphere colloidal suspensions without shear, the flow-arrest transitions are controlled by the volume fraction ϕ and the thermal fluctuations, as the singular interaction potential eliminates temperature. In the non-Brownian limit without thermal fluctuations, the flow-arrest transition occurs near the hard-sphere jamming point at $\phi_J \approx 0.64$, and in the Brownian limit, it takes place at the glass transition density $\phi_G \approx 0.58$ [18, 19]. Near flow-arrest transitions, the shear viscosity η_s apparently diverges as $\eta_s \sim (\phi_m - \phi)^{-\alpha}$, with $\alpha \in [2.2, 2.7]$ in the Brownian limit [20–23] and $\alpha \approx 2.0$ in the non-Brownian limit [18, 24]. Do different arrest points ϕ_m and divergence exponents α imply different underlying physics between the glass and the jamming transitions, as opposed to the unifying view from the jamming diagram?

Part of the answer was revealed in our recent simulation study on the constant stress and pressure rheology of dense colloidal suspensions without HIs [25]. We

found that by imposing constant shear stress σ and pressure Π, instead of fixing the volume fraction ϕ, both the shear viscosity η_s and the incremental normal viscosity η_n' diverge as

$$\{\eta_s, \eta_n'\} = \{k_s, k_n\} \times (\phi_m - \phi)^{-\alpha}, \tag{8.1}$$

where the imposed pressure only affects ϕ_m, and k_s, k_n, and α are constant with $\alpha = 2$. With increasing pressure, the arrest volume fraction ϕ_m increases from ϕ_G towards a point close to the jamming point, defined as the Shear Arrest Point (SAP), $\phi_{\text{SAP}} \approx \phi_J$. Here, $\eta_s = \sigma/\dot{\gamma}$ and $\eta_n' = (\Pi - \Pi^{\text{eq}})/\dot{\gamma}$, with $\dot{\gamma}$ the strain rate and Π^{eq} the equilibrium suspension osmotic pressure at the corresponding ϕ. The results suggested that the physics of jamming dominates the suspension behaviors near the flow-arrest transition, and that thermal fluctuations only affect the arrest point when the pressure, instead of the volume, is held constant. Moreover, although the simulations did not consider HIs, the numerical results agreed well with scaled experimental data [24], implying that the HIs do not qualitatively alter the rheology near flow-arrest transitions, and act in a mean-field fashion. In that study, we did not consider in detail the suspension microstructures and diffusive dynamics.

In this work, we investigate the constant stress and pressure rheology of dense colloidal suspensions near the flow-arrest transition using hydrodynamic simulations. By explicitly computing HIs, we can directly evaluate the influences of HIs on the suspension rheology, structure, and dynamics. Note that the present work and the previous chapter [26] are both motivated by our earlier study [25], with this work focusing on systems with HIs and the other one without HIs.

Hydrodynamic interactions are ubiquitous in colloidal suspensions and can profoundly affect their behavior. For equilibrium suspensions, the dissipative HIs cannot alter the suspension structure, but do strongly affect the short-time transport properties of colloidal suspensions. For instance, in the dilute limit where only pairwise interactions are considered, HIs significantly reduce the short-time self-diffusivity [27] and the instantaneous sedimentation velocity [28]. At higher concentrations, HIs significantly increase the high-frequency dynamic shear viscosity, which diverges near the close packing density due to the diverging near-field lubrication interactions [29, 30].

For sheared suspensions, the influence of HIs is even more profound as they also participate the suspension structural evolution. Rheologically, the structural distortion in sheared suspensions may activate the strong near-field lubrication interactions, which, in turn, increase the hydrodynamic stresses and lead to continuous shear

thickening, i.e., the mild increase in shear viscosity with increasing strain rate, in moderately dense colloidal suspensions [8, 31–33]. Structurally, HIs keep the suspension homogeneous and prevent particles from forming strings aligned in the flow direction at high strain rates [33]. The string phases are always present in simulations without HIs [34, 35], and are also observed in some experiments on hard-sphere suspensions [36, 37]. Moreover, recent confocal microscopy experiments in confined suspensions and scattering experiments in bulk suspensions have found that particles in sheared suspensions align along the vorticity direction and move in a "log-rolling"-like fashion [7, 38–40]. Numerical simulations in confined systems reveal the necessary conditions for such vorticity alignment including HIs and freedom to exchange particles in the velocity gradient direction [38, 41]. However, vorticity alignment has not been observed in simulations with unconfined suspensions. Finally, HIs also affect particle dynamics by introducing chaotic particle trajectories, leading to shear-induced self and collective diffusion even in non-Brownian suspensions [42–44].

Despite their importance in sheared suspension rheology, structure, and dynamics, HIs are difficult to compute because they are long-range and non-pairwise-additive for distant particles and are singular for close particles [45]. Further complications include computing the Brownian forces that satisfy the fluctuation-dissipation relation [46], and introducing size polydispersity to avoid spontaneous crystallization [47, 48]. As a result, existing studies rely on varying degrees of simplification. For example, many studies [5, 49] based on repulsive dense systems assumed that HIs are mean-field-like and completely ignored them [50, 51]. However, for particles in close contact, HIs are distinct from repulsive interactions. Considering two particles separating from each other: the repulsive interaction promotes their departure, while the HIs resist their relative motion away from each other. Others used simplified HIs. For instance, Ando and Skolnick [52] truncated the multipole expansion to the force and torque levels and their simulation method is unsuitable for rheological simulations. Mari et al. [53] completely ignored the far-field HIs in their studies on discontinuous shear thickening. With full HIs, many investigations are limited to monodisperse non-Brownian systems [54, 55]. Dynamic rheology simulations of dense polydisperse colloidal suspensions with the long-range HIs have not therefore been performed.

In this work we use a variant of the Spectral Ewald Accelerated Stokesian Dynamics (SEASD) method [56] as the tool for the computation investigation. The SEASD

is based on the Stokesian Dynamics framework, which captures both the far-field and the near-field HIs by exploiting both the mobility and the resistance formalism of Stokes flow [57]. Features of the SEASD algorithm include $O(N \log N)$ computation scaling via the spectral Ewald method [58, 59], graphic processing unit (GPU) acceleration, and incorporation of particle size polydispersity. To meet the challenges in dynamic simulations of dense suspensions up to the jamming density, we further adopt the near-field Brownian approximation [60], which evaluates Brownian related quantities by assuming mean-field-like far-field HIs, and imposes constant shear stresses and pressures in simulations.

Imposing constant stress and pressure, instead of fixing the strain rate and the volume fraction, is especially suitable for investigating the rheology of dense suspensions. It allows direct assessment of the suspension mechanical responses without a priori assumptions on material behaviors. For suspensions with yield stresses, both the solid-like and liquid-like responses can be accessed. In contrast, imposing a constant strain rate implicitly assumes that the material deforms like a fluid, and therefore can only measure the liquid-like behavior. In addition, increasing the imposed pressures directly identifies the athermal limiting volume fraction without assumptions on the flow-arrest transition. Constant stress and pressure experiments on non-Brownian suspensions identified the limiting volume fraction $\phi_c = 0.585$ [24], which is significantly lower than the jamming density, $\phi_c < \phi_J$. However, analysis on the experimental set up shows that the small gap, of the order of 10 particle diameters, may alter the suspension structures in the shear cell and likely contribute to the low ϕ_c [25, 61]. In the non-Brownian limit, fixing the pressure also reduces the stress fluctuations in the system [62].

Computational realization of the constant stress and pressure rheology requires special considerations, as the dissipative nature of colloidal suspensions prevents the use of many extended ensemble methods in non-equilibrium molecular dynamics [63]. The constraints can be imposed by either introducing physical boundaries with anisotropic volume adjustment, which is often used in studies involving granular materials [64], or by introducing compressibility in the solvent, a new method adopted in our earlier investigation [25]. In this work, we continue with this latter approach, which, for suspensions with HIs, relies on resolving particle interactions in compressible flows [65]. Here, we develop a new algorithm to impose these constraints in hydrodynamic simulations by exploiting the instantaneous nature of HIs. The new algorithm reduces to the constant stress algorithm of Swan and Brady

[66] with fixed volume.

A unifying perspective is emerging on the rheology of both inertia driven granular matter and viscous driven non-Brownian suspensions [24, 67–69]. Despite distinct particle interactions, their rheology is qualitatively similar when the mechanical responses are characterized by a *macroscopic* friction coefficient,

$$\mu = \sigma/\Pi, \tag{8.2}$$

and a flow number defined by the ratio of an internal time scale associated with the system pressure and an external flow time scale $\dot{\gamma}^{-1}$ [70]. Near the jamming transitions, both shear stress σ and particle pressure Π diverge but their ratio μ remain finite. For dry granular materials, the flow number is the inertial number $I = \dot{\gamma} a \sqrt{\rho_p/\Pi}$ with a the particle radius and ρ_p the particle density. The viscous number I_v characterizes the dynamics of non-Brownian viscous suspensions,

$$I_v = \dot{\gamma}\eta_0/\Pi, \tag{8.3}$$

with η_0 the solvent viscosity [24]. For systems exhibiting both the inertial and the viscous driven dynamics, their behaviors can be characterized by combining I and I_v, suggesting a smooth crossover between these two regimes [67]. The similarity between μ-I and μ-I_v rheology means that developments in one system can be applied to both. For example, the non-local formalism of granular rheology [64, 71, 72] can also be used for non-Brownian suspensions. However, it is unclear how particle Brownian motion changes the "granular" perspective. If such an extension were possible, a unified perspective can be established in the Brownian and non-Brownian rheology, allowing significant improvement in the modeling of colloidal suspensions.

In Ref. [25], we adopted the granular perspective to construct a μ-ϕ flow map and identified the SAP $(\phi_{\text{SAP}}, \mu_{\text{SAP}}) = (0.635, 0.16)$ as an intersection between the arrested states and the inaccessible states and discovered the universal viscosity divergences in Eq. (8.1). In this work we continue to use the granular perspective to further characterize the suspension rheology beyond the flow-arrest transitions, hoping to establish a unifying perspective between the Brownian and the non-Brownian rheology, but now with full HIs.

Another focus of this work is on the connection between the suspension macroscopic mechanical response and the diffusive particle dynamics. Perhaps the most obvious connection is the Stokes-Einstein-Sutherland (SES) relation for dilute suspensions,

relating the particle diffusivity to the viscosity and the thermal energy, i.e., $d_0\eta_0/T$ is a constant. This is derived by combining the Einstein relation connecting the single particle diffusivity d_0 and the mobility m_0, $d_0 = k_\mathrm{B}Tm_0$, with $k_\mathrm{B}T$ the thermal energy, and the Stokes drag law for the single particle mobility $m_0 = 6\pi\eta_0 a$ with the particle radius a.

Although derived from the single-particle limit, the SES relation holds well for systems beyond the dilute regime. For equilibrium molecular liquids, the SES relation holds over a wide range of temperatures down to near the glass transition [73, 74]. For equilibrium colloidal suspensions up to the glass transition density, the SES relation remains valid with generalization to the the suspension shear viscosity η_s and the short-time self-diffusivities d_s. For long-time diffusion, mode coupling theory predicts the SES relation remains valid [75, 76], but different interpretations on the experimental results have lead to controversy [48, 77]. Furthermore, the SES relation has also been generalized to viscoelastic medium for microrheology experiments [78, 79]. Near the glass transition, the SES relation breaks down due to the development of dynamic heterogeneity [80]. For systems interacting with very soft potentials, the dynamic heterogeneity is suppressed and the SES relation remains valid at higher density [81–83].

An extended SES relation for non-equilibrium sheared suspensions means that the product of the diffusivity and the suspension shear viscosity is linear to an effective temperature T_eff for *all* volume fractions and *all* strain rates. The existence of such a powerful relation relies on the appropriate choice of T_eff, a concept pioneered by Edwards in the statistical mechanics of granular matter [84]. The effective temperature provides the critical connection between experiments and mean-field theories of dense amorphous systems, such as the soft-glass rheology theory and its mode-coupling variants [85, 86] and the shear-transformation zone theory [87, 88]. Recently, the concept of an effective temperature receives support from the generalized fluctuation-dissipation relations [89], and is consistent among different definitions in athermal [90, 91] and thermal [92–94] systems.

In this work, we explore whether such an extended SES relation exists for sheared suspensions by connecting the suspension diffusive dynamics to its rheology. Existing results are mixed. For sheared amorphous systems, simulations suggest an effective temperature defined from the osmotic compressibility does not lead to the desired data collapse [95]. Experiments on colloidal glasses show that the particle long-time self-diffusivity $d^s_\infty \propto \dot{\gamma}^\beta$ with the exponent $\beta = 1$ [96] or 0.8 [97, 98],

suggesting that $T_{\text{eff}} \propto \sigma\dot{\gamma}^{1-\beta}$. However, these experiments focused on very limited volume fractions and are strongly affected by structural heterogeneity such as shear banding.

This chapter is arranged as follows: After briefly describing our simulation algorithm in Sec. 8.2, we first focus on the features of constant stress and pressure rheology in Sec. 8.3. We then present the rheology of colloidal suspensions from a unifying granular perspective in Sec. 8.4. In Sec. 8.5, we explore the connection among the suspension rheology, structure, and particle diffusion. We summarize and conclude in Sec. 8.6.

8.2 Method

Hydrodynamic interactions in colloidal suspensions

We consider N neutrally-buoyant hard-sphere colloidal particles of different radius a_i located at $\boldsymbol{r}_i$ suspended in a viscous solvent of viscosity η_0 and density ρ_0, occupying a total volume V. The particle radii follow a log-normal distribution, characterized by the volume averaged radius a, such that $a^3 = N^{-1}\sum_i a_i^3$, and a size polydispersity p.d. $= \sigma_a/\overline{a}$, with $\overline{a} = N^{-1}\sum_i a_i$ and $\sigma_a^2 = N^{-1}\sum_i(a_i^2 - \overline{a}^2)$. The radii are sorted into M bins, with an average radius a_α, $\alpha \in \{1, \ldots, M\}$, in each bin. In the thermodynamic limit, both N and V grow unbounded but the number density $n = N/V$ and the volume fraction $\phi = \frac{3}{4}\pi\sum_i a_i^3/V$ remain unchanged.

The dynamics of colloidal particles evolve on a time scale, say t_s, much longer than the particle momentum relaxation time scale τ_I and the hydrodynamic time scale τ_H. The former, $\tau_I = \frac{2}{9}\rho_p a^2/\eta_0$ with ρ_p the particle density, characterizes the time required for the *particle* momentum to dissipate a distance of order the particle size a, and that $t_s \gg \tau_I$ suggests the particle acceleration is negligible over the time scale t_s and the dynamics are overdamped. The hydrodynamic time scale, $\tau_H = \rho_0 a^2/\eta_0$, describes the time required for the *solvent* momentum to diffusive the same distance, and that $t_s \gg \tau_H$ means the Reynolds number $\text{Re} = \tau_H/t_s \ll 1$. Therefore, the HIs among the particles are dominated by the viscous stresses, and the fluid velocity $\boldsymbol{v}(\boldsymbol{x})$ and the pressure $p(\boldsymbol{x})$ are governed by Stokes equation,

$$\boldsymbol{\nabla} p(\boldsymbol{x}) = \eta_0 \nabla^2 \boldsymbol{v}(\boldsymbol{x}) \text{ and } \boldsymbol{\nabla}\cdot\boldsymbol{v}(\boldsymbol{x}) = 0, \tag{8.4}$$

supplemented by no-slip boundary conditions $\boldsymbol{v} = \boldsymbol{U}_i + \boldsymbol{\Omega}_i \times (\boldsymbol{x} - \boldsymbol{r}_i)$ at the surface of particle i with velocity $\boldsymbol{U}_i$ and angular velocity $\boldsymbol{\Omega}_i$.

Because of the linearity of Eq. (8.4), the fluid forces and their moments, i.e., the force $\boldsymbol{F}^{\text{H}}$, torque $\boldsymbol{T}^{\text{H}}$, and stresslets $\boldsymbol{S}^{\text{H}}$, are linear to the particle kinematics including

the velocity $\boldsymbol{U}$ and the angular velocity $\boldsymbol{\Omega}$. This leads to the resistance formalism,

$$\begin{bmatrix} \boldsymbol{\mathcal{F}}^{\mathrm{H}} \\ \boldsymbol{S}^{\mathrm{H}} \end{bmatrix} = -\boldsymbol{\mathcal{R}} \cdot \begin{bmatrix} \boldsymbol{\mathcal{U}} - \boldsymbol{\mathcal{U}}^{\infty} \\ -\boldsymbol{E}^{\infty} \end{bmatrix} \tag{8.5}$$

where $\boldsymbol{\mathcal{F}}^{\mathrm{H}} = (\boldsymbol{F}^{\mathrm{H}}, \boldsymbol{T}^{\mathrm{H}})^{\dagger}$ is the generalized force, $\boldsymbol{\mathcal{U}} - \boldsymbol{\mathcal{U}}^{\infty} = (\boldsymbol{U} - \boldsymbol{U}^{\infty}, \boldsymbol{\Omega} - \boldsymbol{\Omega}^{\infty})^{\dagger}$ is the generalized velocity difference with respect to $\boldsymbol{U}^{\infty}$, $\boldsymbol{\Omega}^{\infty}$, and $\boldsymbol{E}^{\infty}$ from the imposed velocity field $\boldsymbol{v}^{\infty}$, *i.e.*, for particle i, $\boldsymbol{U}_i^{\infty} = \boldsymbol{v}^{\infty}(\boldsymbol{r}_i)$, $\boldsymbol{\Omega}_i^{\infty} = \frac{1}{2}\boldsymbol{\nabla}\times\boldsymbol{v}^{\infty}|_{\boldsymbol{r}_i}$, and $\boldsymbol{E}_i^{\infty} = \frac{1}{2}[\boldsymbol{\nabla}\boldsymbol{v}^{\infty} + (\boldsymbol{\nabla}\boldsymbol{v}^{\infty})^{\dagger}]_{\boldsymbol{r}_i}$. Here, the dagger represents transpose and symbols without subscript suggest the entire suspension, *e.g.*, $\boldsymbol{U} = (\boldsymbol{U}_1, \boldsymbol{U}_2, \ldots, \boldsymbol{U}_N)^{\dagger}$. The grand resistance tensor $\boldsymbol{\mathcal{R}}$ depends only on the suspension configuration $\boldsymbol{r}$, and can be conveniently partitioned as

$$\boldsymbol{\mathcal{R}}(\boldsymbol{r}) = \begin{bmatrix} \boldsymbol{R}_{\mathcal{F}\mathcal{U}} & \boldsymbol{R}_{\mathcal{F}\mathrm{E}} \\ \boldsymbol{R}_{\mathrm{S}\mathcal{U}} & \boldsymbol{R}_{\mathrm{SE}} \end{bmatrix}, \tag{8.6}$$

where, for example, $\boldsymbol{R}_{\mathcal{F}\mathcal{U}}$ describes the coupling between the generalized force $\boldsymbol{\mathcal{F}}$ to the generalized velocity difference $\boldsymbol{\mathcal{U}} - \boldsymbol{\mathcal{U}}^{\infty}$.

The overdamped Langevin equation describes the dynamics of colloidal particles,

$$0 = \boldsymbol{\mathcal{F}}^{\mathrm{H}} + \boldsymbol{\mathcal{F}}^{\mathrm{P}} + \boldsymbol{\mathcal{F}}^{\mathrm{B}}, \tag{8.7}$$

where $\boldsymbol{\mathcal{F}}^{\mathrm{P}}$ is the generalized force from interparticle conservative potentials, and $\boldsymbol{\mathcal{F}}^{\mathrm{B}}$ is the stochastic Brownian force satisfying the fluctuation-dissipation relation

$$\overline{\boldsymbol{\mathcal{F}}^{\mathrm{B}}(t)} = 0 \text{ and } \overline{\boldsymbol{\mathcal{F}}^{\mathrm{B}}(t)\boldsymbol{\mathcal{F}}^{\mathrm{B}}(0)} = 2k_{\mathrm{B}}T\boldsymbol{R}_{\mathcal{F}\mathcal{U}}\delta(t). \tag{8.8}$$

With Eq. (8.5), the suspension configuration change $\Delta\boldsymbol{\mathcal{X}}$, including both the translational and rotational degrees of freedom, over a small time Δt, can be solved by integrating Eq. (8.7) as

$$\Delta\boldsymbol{\mathcal{X}} = \left[\boldsymbol{\mathcal{U}}^{\mathrm{E}} + \boldsymbol{\mathcal{U}}^{\mathrm{B}} + \boldsymbol{\mathcal{U}}^{\mathrm{P}}\right]\Delta t + \Delta\boldsymbol{\mathcal{X}}^{\mathrm{B}}, \tag{8.9}$$

where $\Delta\boldsymbol{\mathcal{X}}^{\mathrm{B}}$ is the stochastic Brownian displacement satisfying

$$\overline{\Delta\boldsymbol{\mathcal{X}}^{\mathrm{B}}} = 0 \text{ and } \overline{\Delta\boldsymbol{\mathcal{X}}^{\mathrm{B}}\Delta\boldsymbol{\mathcal{X}}^{\mathrm{B}}} = 2k_{\mathrm{B}}T\Delta t\boldsymbol{R}_{\mathcal{F}\mathcal{U}}^{-1}, \tag{8.10}$$

and $\boldsymbol{\mathcal{U}}^{\mathrm{E}}$, $\boldsymbol{\mathcal{U}}^{\mathrm{P}}$, and $\boldsymbol{\mathcal{U}}^{\mathrm{B}}$ are, respectively, the deterministic velocity contributions from the imposed flow, the interparticle force, and the Brownian drift:

$$\boldsymbol{\mathcal{U}}^{\mathrm{E}} = \boldsymbol{\mathcal{U}}^{\infty} + \boldsymbol{R}_{\mathcal{F}\mathcal{U}}^{-1} \cdot \boldsymbol{R}_{\mathcal{F}\mathrm{E}} \cdot \boldsymbol{E}^{\infty}, \tag{8.11}$$

$$\boldsymbol{\mathcal{U}}^{\mathrm{P}} = \boldsymbol{R}_{\mathcal{FU}}^{-1} \cdot \boldsymbol{\mathcal{F}}^{\mathrm{P}}, \tag{8.12}$$

$$\boldsymbol{\mathcal{U}}^{\mathrm{B}} = k_{\mathrm{B}}T\boldsymbol{\nabla} \cdot \boldsymbol{R}_{\mathcal{FU}}^{-1}. \tag{8.13}$$

Note that $\boldsymbol{\mathcal{U}}^{\mathrm{B}}$ arises due to the configuration dependent Brownian force $\boldsymbol{\mathcal{F}}^{\mathrm{B}}$, and the divergence operator in Eq. (8.13) acts on the last index of $\boldsymbol{R}_{\mathcal{FU}}^{-1}$.

Spatially averaging the Cauchy stress in the suspension leads to the suspension total stress without the fluid thermodynamic pressure [99, 100],

$$\begin{aligned}\langle \boldsymbol{\Sigma} \rangle =& 2\eta_0 \langle (\boldsymbol{E}^{\infty})' \rangle + (\kappa_0 - \tfrac{2}{3}\eta_0) E^{\infty} \boldsymbol{I} \\ & - nk_{\mathrm{B}}T\boldsymbol{I} + n(\langle \boldsymbol{S}^{\mathrm{E}} \rangle + \langle \boldsymbol{S}^{\mathrm{P}} \rangle + \langle \boldsymbol{S}^{\mathrm{B}} \rangle),\end{aligned} \tag{8.14}$$

where the average operator $\langle \cdot \rangle = V^{-1} \sum_i (\cdot)_i$, the traceless strain rate $(\boldsymbol{E}^{\infty})'$ and the rate of expansion E^{∞} satisfy $(\boldsymbol{E}^{\infty})' + \frac{1}{3}E^{\infty}\boldsymbol{I} = \boldsymbol{E}^{\infty}$, κ_0 is the solvent bulk viscosity, and the superscripts in $\langle \boldsymbol{S}^{\mathrm{E}} \rangle$, $\langle \boldsymbol{S}^{\mathrm{P}} \rangle$, and $\langle \boldsymbol{S}^{\mathrm{B}} \rangle$ have the same meaning as those in Eq. (8.10). Here, the solvent is compressible for imposing the constant pressure constraint. The stresslets are computed from the resistance tensors,

$$\langle \boldsymbol{S}^{\mathrm{E}} \rangle = -\langle \boldsymbol{R}_{\mathrm{S}\mathcal{U}} \cdot \boldsymbol{R}_{\mathcal{FU}}^{-1} \cdot \boldsymbol{R}_{\mathcal{F}\mathrm{E}} - \boldsymbol{R}_{\mathrm{SE}} \rangle : \langle \boldsymbol{E}^{\infty} \rangle, \tag{8.15}$$

$$\langle \boldsymbol{S}^{\mathrm{P}} \rangle = -\langle (\boldsymbol{R}_{\mathrm{S}\mathcal{U}} \cdot \boldsymbol{R}_{\mathcal{FU}}^{-1} + r\mathbf{l}) \cdot \boldsymbol{F}^{\mathrm{P}} \rangle, \tag{8.16}$$

$$\langle \boldsymbol{S}^{\mathrm{B}} \rangle = -k_{\mathrm{B}}T\langle \boldsymbol{\nabla} \cdot (\boldsymbol{R}_{\mathrm{S}\mathcal{U}} \cdot \boldsymbol{R}_{\mathcal{FU}}^{-1}) \rangle, \tag{8.17}$$

where the divergence operator in Eq. (8.17) acts on the last index in the parenthesis. Accordingly, the suspension shear viscosity is decomposed as

$$\eta_s = \eta_0 + \eta^{\mathrm{E}} + \eta^{\mathrm{B}} + \eta^{\mathrm{P}}. \tag{8.18}$$

Note that for hard-sphere colloidal suspensions, the first and the second terms in Eq. (8.16) cancel exactly, and therefore interparticle force contribution to the stresslet is zero [99].

The constant stress and pressure dynamics

In a simple shear flow, the imposed velocity field $\boldsymbol{v}^{\infty} = (\dot{\gamma}x_2, 0, 0)$, where $\dot{\gamma}$ is the strain rate and $\boldsymbol{x} = (x_1, x_2, x_3)$ is the position in the 1- (the velocity), 2- (the velocity gradient), and 3- (the vorticity) direction. The suspension dynamics and mechanics can be respectively solved from Eq. (8.9) and (8.14).

For simulations with constant imposed shear stress σ and pressure Π, we solve for the corresponding strain rate $\dot{\gamma}$ and expansion rate $\dot{e}$, which lead to $\boldsymbol{v}^{\infty}(\boldsymbol{x})$ and the configuration evolution in Eq. (8.9). The computation exploits the instantaneous

nature of the Stokes equations and proceeds as follows: At each time t with the suspension configuration $\boldsymbol{r}(t)$, the resistance tensors in Eq. (8.6) are known. We first evaluate the velocity and stress contributions from the interparticle force, $\boldsymbol{S}^{\mathrm{P}}$ and $\boldsymbol{\mathcal{U}}^{\mathrm{P}}$, and the Brownian motion, $\boldsymbol{S}^{\mathrm{B}}$, $\boldsymbol{\mathcal{U}}^{\mathrm{B}}$, and $\Delta\boldsymbol{\mathcal{X}}^{\mathrm{B}}$. The suspension is then subjected to two unit test flows, $\hat{\boldsymbol{v}}_{\gamma}^{\infty} = (x_2, 0, 0)$ and $\hat{\boldsymbol{v}}_{e}^{\infty} = \frac{1}{3}(x_1, x_2, x_3)$. From the linearity of Stokes flow, with an imposed flow $\boldsymbol{v}^{\infty} = \dot{\gamma}\hat{\boldsymbol{v}}_{\gamma}^{\infty} + \dot{e}\hat{\boldsymbol{v}}_{e}^{\infty}$, the flow stresslet

$$\boldsymbol{S}^{\mathrm{E}} = \dot{\gamma}\hat{\boldsymbol{S}}_{\gamma}^{\mathrm{E}} + \dot{e}\hat{\boldsymbol{S}}_{e}^{\mathrm{E}}, \tag{8.19}$$

where, $\hat{\boldsymbol{S}}_{\gamma}^{\mathrm{E}}$ is from $\hat{\boldsymbol{v}}_{\gamma}^{\infty}$ and $\hat{\boldsymbol{S}}_{e}^{\mathrm{E}}$ is from $\hat{\boldsymbol{v}}_{e}^{\infty}$. From Eq. (8.14), the suspension shear stress and pressure balances are

$$\sigma = \dot{\gamma}\eta_0 + n(\dot{\gamma}\hat{S}_{\gamma,12}^{\mathrm{E}} + \dot{e}\hat{S}_{e,12}^{\mathrm{E}} + S_{12}^{\mathrm{P}} + S_{12}^{\mathrm{B}}), \tag{8.20}$$

$$-\Pi = \kappa_0\dot{e} - nk_{\mathrm{B}}T + \tfrac{1}{3}n(\dot{\gamma}\hat{S}_{\gamma}^{\mathrm{E}} + \dot{e}\hat{S}_{e}^{\mathrm{E}} + S^{\mathrm{P}} + S^{\mathrm{B}}), \tag{8.21}$$

where, for example, S_{12}^{B} is the 12-component of $\left\langle \boldsymbol{S}^{\mathrm{B}} \right\rangle$ and $S^{\mathrm{B}} = \boldsymbol{I} : \left\langle \boldsymbol{S}^{\mathrm{B}} \right\rangle$. Therefore, we solve for $\dot{\gamma}$ and $\dot{e}$ from Eq. (8.20) and (8.21), and reconstruct $\boldsymbol{S}^{\mathrm{E}}$ from Eq. (8.19). To advance the particle dynamics, we use Eq. (8.9) with

$$\boldsymbol{\mathcal{U}}^{\mathrm{E}} = \dot{\gamma}\,\hat{\boldsymbol{\mathcal{U}}}_{\gamma}^{\mathrm{E}} + \dot{e}\,\hat{\boldsymbol{\mathcal{U}}}_{e}^{\mathrm{E}}, \tag{8.22}$$

where $\hat{\boldsymbol{\mathcal{U}}}_{\gamma}^{\mathrm{E}}$ is from $\hat{\boldsymbol{v}}_{\gamma}^{\infty}$ and $\hat{\boldsymbol{\mathcal{U}}}_{e}^{\mathrm{E}}$ is from $\hat{\boldsymbol{v}}_{e}^{\infty}$. The size of the simulation box L, with $V = L^3$, is adjusted according to $\mathrm{d}L/\mathrm{d}t = \frac{1}{3}\dot{e}L$.

The constant stress and constant pressure method above is an extension of the method of Wang and Brady [25] for simulations without HIs. Our method reduces to the constant stress and fixed volume method of Swan and Brady [66] when $\dot{e} = 0$.

In this work, we focus on polydisperse suspensions with size polydispersity p.d. = 0.1, particle number $N = 100$, and the species number $M = 10$. In the constant stress and pressure simulations, the suspension dynamics are controlled by the stress Péclet number Pe_{σ} and the dimensionless pressure $\bar{\Pi}$,

$$\mathrm{Pe}_{\sigma} = \sigma a^2/(\eta_0 d_0) \quad \text{and} \quad \bar{\Pi} = \Pi a^3/(k_{\mathrm{B}}T), \tag{8.23}$$

with the single particle diffusivity $d_0 = k_{\mathrm{B}}T/(6\pi\eta_0 a)$. The stress Péclet number Pe_{σ} is connected to the strain rate Péclet number $\mathrm{Pe}_{\dot{\gamma}}$ as

$$\mathrm{Pe}_{\dot{\gamma}} = (\eta_0/\eta_s)\mathrm{Pe}_{\sigma} = \dot{\gamma}a^2/d_0. \tag{8.24}$$

To resolve the dynamics, the time is scaled with a^2/d_0 when $\mathrm{Pe}_{\sigma} \le 1$ and with η_0/σ when $\mathrm{Pe}_{\sigma} > 1$. For each combination of (σ, Π), we perform a long simulation at

the corresponding $(\mathrm{Pe}_\sigma, \bar{\Pi})$ with a dimensionless time $\tau = 5000$ and a step size $\Delta\tau = 10^{-2}$ for $\bar{\Pi} < 100$ and $\Delta\tau = 2.5 \times 10^{-3}$ for $\bar{\Pi} \geq 100$. The simulations start with random configurations generated by the polydisperse Lubachevsky-Stillinger algorithm [101, 102]. When computing the results, the data from the first $\tau = 1000$ are discarded. In the appendix we describe the computation of HIs using the SEASD method with near-field Brownian approximation, and the algorithm validation using the constant stress computations.

A feature of the constant stress simulations is that, with a fixed time step at $\mathrm{Pe}_\sigma > 1$, the temporal resolution of the configuration evolution improves automatically with increasing suspension shear viscosity. This is because the step size $\Delta\tau = \Delta t\sigma/\eta_0 = \Delta\gamma(\eta_s/\eta_0)$, where the strain step $\Delta\gamma = \dot{\gamma}\Delta t$ characterizes the temporal resolution. Therefore, the same dimensionless time step $\Delta\tau$ may be used for both the solid-like and the liquid-like suspensions. In contrast, with fixed $\dot{\gamma}$, it is necessary to reduce the step size near the flow-arrest transitions to resolve the configuration evolution. In addition, larger time steps can be used in constant stress simulations. For example, when the shear viscosity $\eta_s/\eta_0 \approx 10$, typical for suspensions at $\phi \approx 0.45$ [33], $\Delta\tau = 10^{-2}$ with constant stress is equivalent to $\Delta\gamma = 10^{-3}$, a typical step size in constant strain rate studies [44, 54].

Furthermore, to prevent singular particle overlap in dynamic simulations with constant time step $\Delta\tau$, we introduce an additional excluded volume radius $b_i > a_i$ for each particle. Here, the excluded volume parameter $\delta = 1 - a_i/b_i = 5 \times 10^{-4}$, corresponding to a 1.5×10^{-3} change in volume fractions. From simulations on bidisperse suspensions [56], introducing δ does not change the suspension rheology at low to moderate $\mathrm{Pe}_{\dot{\gamma}}$, but slightly reduces the shear viscosity when $\mathrm{Pe}_{\dot{\gamma}} \gg 1$. In this work we enforce the excluded volume condition using the potential-free algorithm [34, 103], and monitor the stress contribution from the excluded volume effects. To minimize the impact of this procedure, a simulation is valid only if the excluded volume effect contributes less than 1% to the total stress.

8.3 Features of constant stress and pressure rheology

In this section we focus on the features of constant stress and pressure rheology at two imposed pressures, $\bar{\Pi} = 1.5$ and 50. At low imposed pressure, e.g., $\bar{\Pi} = 1.5$, colloidal suspensions flow like a liquid and do not exhibit a yield stress. With high imposed pressure, e.g., $\bar{\Pi} = 50$, the suspensions become glassy and develop a yield stress, i.e., they flow only if the imposed stress exceeds the yield stress.

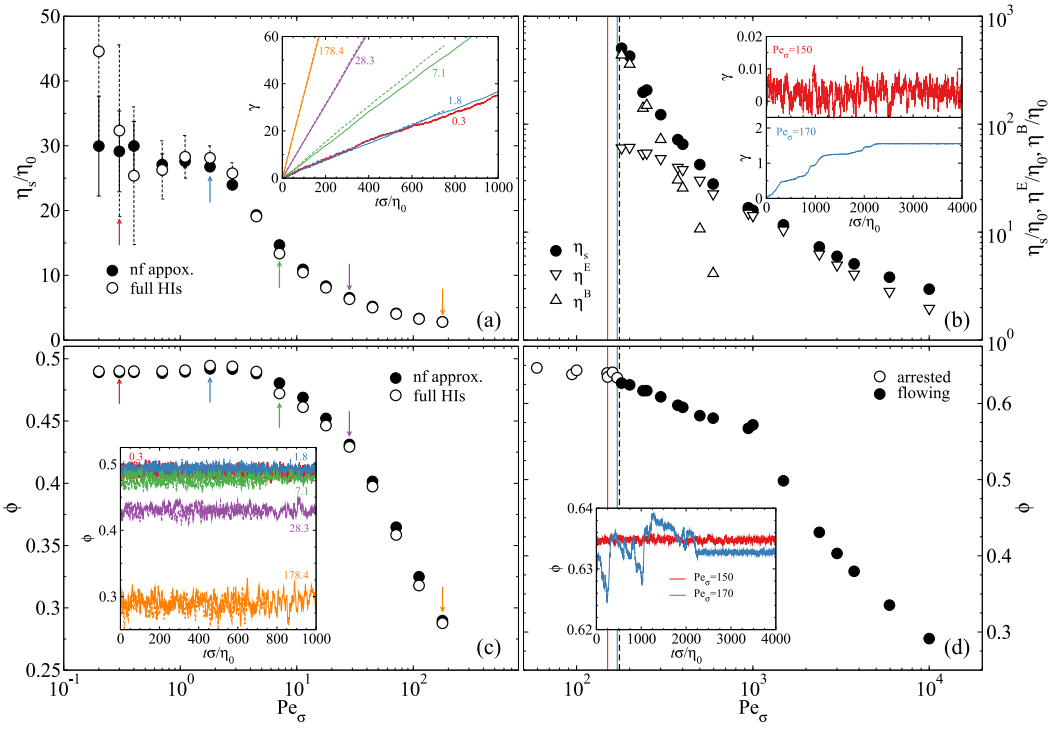

Figure 8.1: (Color Online) The constant stress and pressure rheology of a polydisperse suspension with polydispersity p.d. = 0.1 as functions of Pe_σ at $\bar{\Pi} = 1.5$ [(a), (c)] and at $\bar{\Pi} = 50$ [(b), (d)]. In (a) and (c), the results with full HIs are shown in open symbols in the main figure and dashed lines in the inset, and the results with near-field Brownian approximation are shown in filled symbols and solid lines. In (b) and (d), the thin lines indicate the Pe_σ for the insets with corresponding colors, and the black dashed line outlines the flow-arrest transition. (a) The suspension shear viscosity η_s/η_0. Inset: the time evolution of the accumulated strains γ at $\mathrm{Pe}_\sigma = 0.3$, 1.8, 7.1, 28.3, and 178.4. (b) The suspension shear viscosity η_s/η_0 (filled circle), the Brownian contribution η^{B}/η_0 (up triangle) and the flow contribution η^{E}/η_0 (down triangle). Insets: time trace of the accumulated strain γ at $\mathrm{Pe}_\sigma = 150$ and 170. (c) The steady state volume fraction ϕ. Inset: time traces of the instantaneous volume fraction at the same Pe_σ as (a). (d) The steady state volume fraction ϕ. The arrested results are shown in open circles and the flowing results in filled circles. Inset: time trace of the volume fraction ϕ at $\mathrm{Pe}_\sigma = 150$ and 170.

Rheology: shear viscosity and volume fraction

Fig. 8.1 presents the suspension rheological behaviors in shear viscosity η_s and volume fraction ϕ. The shear viscosity is the ratio of the imposed stress σ and the mean strain rate $\langle\dot{\gamma}\rangle$, i.e., $\eta_s = \sigma/\langle\dot{\gamma}\rangle$. The error bars in Fig. 8.1 are estimated by splitting the long simulations runs into independent segments of 500 dimensionless time units each. The liquid-like results at $\bar{\Pi} = 1.5$ are shown in Fig. 8.1a and 8.1c,

and the glassy results at $\bar{\Pi} = 50$ are shown in Fig. 8.1b and 8.1d.

We begin with liquid-like suspensions at $\bar{\Pi} = 1.5$. Fig. 8.1a shows the shear viscosity η_s/η_0 as a function of the stress Péclet number Pe_σ. Despite some fluctuations, in the $\mathrm{Pe}_\sigma \to 0$ limit, the shear viscosity η_s approaches a finite value corresponding to the zero-shear viscosity of an equilibrium suspension with the same osmotic pressure as the imposed pressure Π. With increasing Pe_σ, η_s decreases continuously, and quickly approaches the solvent viscosity, i.e., $\eta_s \to \eta_0$ as $\mathrm{Pe}_\sigma \to \infty$. The lack of shear-thickening and a finite high-shear viscosity are the key features of the constant stress and pressure rheology as the suspension dilates with growing Pe_σ. This is because the imposed pressure is scaled with $k_\mathrm{B}T$, but the suspension pressure scales as $f(\phi)\eta_0\dot{\gamma}$, with the function $f(\phi) \sim \phi^2$ at small ϕ, and therefore the suspension dilates so the pressure matches the imposed value.

The inset of Fig. 8.1a presents the time trace of the accumulated strain $\gamma(t) = \int_0^t \dot{\gamma}(\tau)d\tau$ for several Pe_σ. For continuously deforming, liquid-like suspensions, $\gamma(t)$ increases linearly with time. The inverse slope of the accumulated strain with respect to the dimensionless time $t\sigma/\eta_0$ is the suspension shear viscosity η_s/η_0. Therefore, the higher the suspension shear viscosity, the slower γ increases with time. For suspensions with similar shear viscosities, e.g., $\mathrm{Pe}_\sigma = 0.3$ and 1.8, their accumulated strains almost overlap. The accumulated strain $\gamma(t)$ exhibits more fluctuations at low Pe_σ relative to results at high Pe_σ due to stronger thermal fluctuations.

Fig. 8.1c shows the steady state volume fraction ϕ as a function of Pe_σ, and the inset presents the time trace of the instantaneous ϕ. When $\mathrm{Pe}_\sigma < 1$, changing Pe_σ does not significantly alter ϕ, and in the $\mathrm{Pe}_\sigma \to 0$ limit, the volume fraction ϕ corresponds that of an equilibrium suspension with an osmotic pressure equal to the imposed pressure. At higher Pe_σ, increasing Pe_σ reduces ϕ because the suspension dilates in response to the increase in suspension pressure from the growing imposed stress. The reduction in ϕ is drastic with respect to Pe_σ: at $\mathrm{Pe}_\sigma = 178$, the volume fraction has already decreased from ~ 0.49 to below 0.3. The inset of Fig. 8.1c shows that the volume fraction for all cases fluctuates around a constant value, confirming that the suspension is at steady sate. Moreover, the fluctuations in ϕ are more significant at lower ϕ, due to the lower suspension bulk viscosity [104]. As the bulk viscosity characterizes the suspension's resistance to expansion, lower volume fraction makes responding to an imposed pressure easier for the suspension, and therefore allows larger fluctuations.

Fig. 8.1a and 8.1c also compare the results from full hydrodynamic computations (open symbols and dashed lines) and near-field Brownian approximations (filled symbols and solid lines). Despite small quantitative differences, the two methods agree well with each other. This is consistent with the results in constant ϕ and $\dot{\gamma}$ simulations in bidisperse suspensions [56]. Considering the tremendous time saving from the near-field Brownian approximation, it is adequate for the constant stress and pressure dynamic simulations of polydisperse suspensions in this work.

When the imposed pressure $\bar{\Pi} > 3$, the colloidal suspension becomes glassy and a yield stress emerges without apparent structural signatures. Note that at equilibrium, $\bar{\Pi} = 3$ corresponds to $\phi \approx 0.56$. Therefore, the suspension shear viscosity η_s diverges at low imposed stress. Determining the exact value of the yield stress is difficult as it depends on the observation time scale—the longer one waits, the more likely for one to observe flow [16]. In practice, however, the flow-arrest transition can be determined by a viscosity threshold, beyond which the suspension is considered arrested. Here, the threshold viscosity is $\eta_s/\eta_0 = 2000$. For typical simulations with dimensionless time $\tau = 5000$, this viscosity threshold corresponds to a minimum strain $\gamma \approx 2.5$ for the flowing suspensions at $\mathrm{Pe}_\sigma > 1$.

Fig. 8.1b and 8.1d illustrate the constant stress and pressure rheology of glassy suspensions at $\bar{\Pi} = 50$. Fig. 8.1b presents the various components of the shear viscosity. From the simulations, the yield stres corresponding to $\mathrm{Pe}_\sigma \approx 175$ is shown as a dashed vertical line in the figures. When the imposed stress is lower than the yield stress, the suspension is arrested and unable to flow. This is confirmed in the time traces of the accumulated strain γ at $\mathrm{Pe}_\sigma = 150$ and 170 in the inset of Fig. 8.1b. When close to the yield stress, e.g., at $\mathrm{Pe}_\sigma = 170$, the suspension appears unstable, switching between flowing and arrested behaviors. In this case, the computed viscosity exhibits large fluctuations. Further reducing the imposed stress, the suspension becomes completely arrested. In the inset of Fig. 8.1b, the accumulated strain cannot exceed 0.01 at $\mathrm{Pe}_\sigma = 150$ even over an extended period time of $t\sigma/\eta_0 = 4000$.

The shear viscosity η_s/η_0 in flowing suspensions shows strong shear thinning in Fig. 8.1b. Over two decades of Pe_σ the viscosity reduces more than three orders of magnitude. The Brownian viscosity η^{B}, shown as up triangles, is responsible for the strong shear-thinning behaviors near the flow-arrest transition. The flow viscosity η^{E}, shown as down triangles, changes more slowly compared to η^{B} near the flow arrest transition. At higher Pe_σ, η^{E} also decreases with increasing Pe_σ, and the

shear thinning of η^{E} with growing Pe_σ is much weaker comparing to η^{B}. Unlike the constant volume simulations where η^{E} reaches a high-shear rate limiting value, the decrease in η^{E} in constant stress and pressure rheology results from dilation of the suspension.

Fig. 8.1d presents the suspension volume fraction ϕ as functions of Pe_σ at $\bar{\Pi} = 50$. Here, the volume fractions at the arrest state are shown in open symbols and the flowing state in filled symbols. In Fig. 8.1d, with increasing Pe_σ, the suspension always dilates regardless of flowing or not from $\phi \approx 0.645$ at $\mathrm{Pe}_\sigma \approx 60$ to less than 0.3 at $\mathrm{Pe}_\sigma = 10^4$. The dilation before flow is necessary in order for the suspension to rearrange its structure and to allow two particles to pass each other. Furthermore, the volume fraction shows a kink near $\mathrm{Pe}_\sigma = 10^3$ at $\phi \approx 0.57$. After $\mathrm{Pe}_\sigma = 10^3$, the dilation becomes stronger with increasing Pe_σ. The kink in ϕ at $\mathrm{Pe}_\sigma = 10^3$ is not observed for suspensions at lower imposed pressures, e.g., in Fig. 8.1c at $\bar{\Pi} = 1.5$. From the structural examinations in Sec. 8.3, we found that this kink is related to the shear-induced string formation in polydisperse suspensions.

The time traces of the ϕ for arrested suspensions, also at $\mathrm{Pe}_\sigma = 150$ and 170, are shown in the inset of Fig. 8.1d. Far from the flow-arrest transition, i.e., at $\mathrm{Pe}_\sigma = 150$, ϕ fluctuates with small variation. Near the flow-arrest transition, i.e., at $\mathrm{Pe}_\sigma = 170$, ϕ also show intermittent behaviors and becomes unstable when the corresponding accumulated strain γ exhibits significant increases in the inset of Fig. 8.1b. The unstable behaviors stop when γ stops growing at $t\sigma/\eta_0 \gtrsim 2200$.

Structures: the pair distribution function

We investigate the suspension structure by computing the steady state pair distribution function

$$g(\boldsymbol{r}) = \frac{V}{N^2}\left\langle \sum_{i,j}{}' \delta(\boldsymbol{r} - \boldsymbol{r}_i + \boldsymbol{r}_j)\right\rangle, \tag{8.25}$$

where the prime on the summation excludes the case of $i = j$, and $\delta(x)$ is the Dirac delta function. It is the conditional probability of finding a second particle at location $\boldsymbol{r}$ given the first particle. Fig. 8.2 shows the equatorial slices of $g(\boldsymbol{r})$ with width $0.7a$ on the velocity-velocity gradient (12), velocity-vorticity (13), and velocity gradient-vorticity (23) planes for suspensions with $\bar{\Pi} = 1.5$ at selected Pe_σ. Changing the width of the slice has little qualitative influences on the results. With HIs, the suspension remains homogeneous for all Pe_σ. This is distinct from simulations without HIs, where the particles spontaneously align in the velocity direction, forming string-like structures at high Pe_σ. In the shear plane, $g_{12}(\boldsymbol{r})$ is

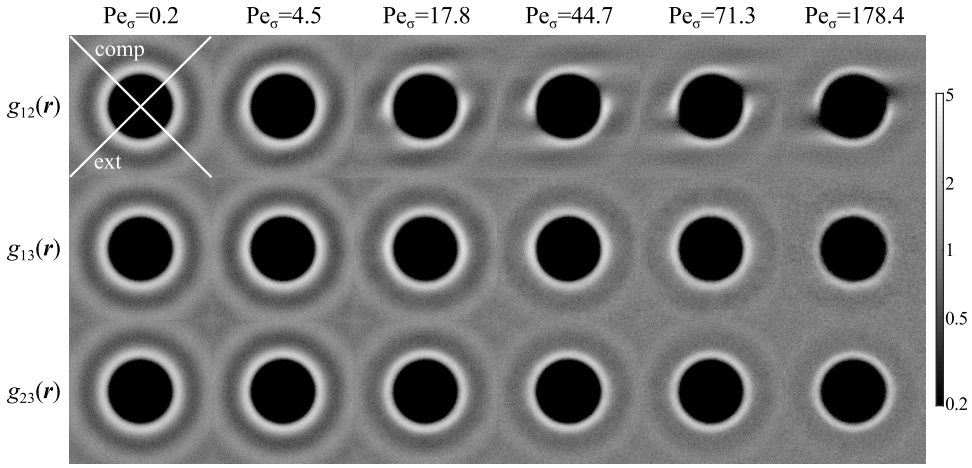

Figure 8.2: Equatorial slices of the pair distribution function $g(\boldsymbol{r})$ on the velocity-velocity gradient (12), velocity-vorticity (13), and velocity gradient-vorticity (23) planes of suspensions with an imposed pressure $\bar{\Pi} = 1.5$ at various Pe_σ. The suspension size polydispersity p.d. = 0.1. The width of the slice is $0.7a$. The compression and the extension axes are also highlighted.

almost isotropic at $\mathrm{Pe}_\sigma = 0.2$. With increasing Pe_σ, for example, at $\mathrm{Pe}_\sigma = 17.8$, the neighboring particles begin to accumulate at the particle front in the flow direction, suggesting the formation of a particle pair. The pair then rotates, first quickly in the compressional quadrant, as indicated by the lower probability density near the compressional axis, and then slowly in the extensional quadrant. Near the extensional axis, the particle pair disengages. Further increase in Pe_σ compresses the first ring of $g_{12}(\boldsymbol{r})$, suggesting a boundary layer formation [105]. However, the overall intensity of $g_{12}(\boldsymbol{r})$ decreases with increasing Pe_σ due to the suspension dilation. Moreover, a particle depletion wake emerges near the extensional axis when $\mathrm{Pe}_\sigma > 44.7$ because, compared to the flow, the diffusion is too weak to drive the particles towards the low density region.

In Fig. 8.2, the $g(\boldsymbol{r})$ slices in the 13-plane, $g_{13}(\boldsymbol{r})$, exhibit weaker anisotropy compared to $g_{12}(\boldsymbol{r})$. Starting from an isotropic structure at $\mathrm{Pe}_\sigma = 0.2$, $g_{13}(\boldsymbol{r})$ first show particle accumulation in the velocity direction (left-right in the figure) relative to the vorticity direction (up-down in the figure) with increasing Pe_σ. This is especially pronounced at $\mathrm{Pe}_\sigma = 44.7$. However, at higher Pe_σ, this trend is reversed along with the formation of depletion wake in $g_{12}(\boldsymbol{r})$. For example, at $\mathrm{Pe}_\sigma = 178$, slightly more particles are present in the vorticity direction compared to the velocity direction, suggesting the a weak particle alignment in the vorticity direction. Finally, the $g(\boldsymbol{r})$ slice in the 23-plane, $g_{23}(\boldsymbol{r})$, is always isotropic. At $\bar{\Pi} = 1.5$, the principle influence

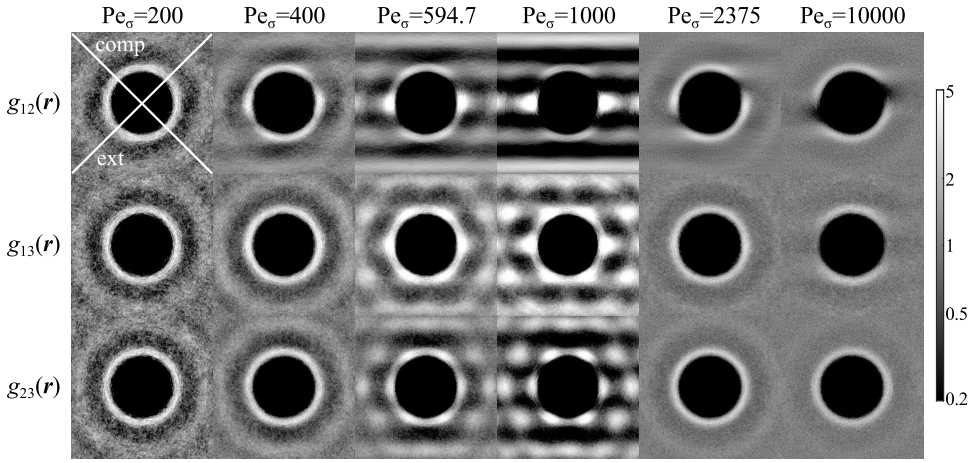

Figure 8.3: Equatorial slices of pair distribution function $g(\boldsymbol{x})$ on the 12-, 13-, and 23-planes of suspensions with imposed pressure $\bar{\Pi} = 50$ at various Pe_σ. Other parameters are identical to Fig. 8.2.

of increasing Pe_σ on $g_{23}(\boldsymbol{r})$ is the reducing suspension structural features beyond the nearest neighbors and the decreasing peak values associated with the nearest neighbors.

Fig. 8.3 presents the equatorial slices of $g(\boldsymbol{r})$ for suspensions at $\bar{\Pi} = 50$. As indicated in Fig. 8.1d, the at-rest volume fraction at this imposed pressure is well above the monodisperse fluid-solid phase transition, and therefore the colloidal suspension is prone to crystallization. At the lowest Pe_σ in Fig. 8.3, the suspension structure is isotropic without indications of structural formation, suggesting that introducing a small size polydispersity effectively suppresses the spontaneous crystallization.

Increasing Pe_σ reveals that the size polydispersity p.d. = 0.1 is not sufficient to prevent formation of string phases at intermediate Pe_σ, i.e., at $\mathrm{Pe}_\sigma = 595$ and 1000 in Fig. 8.3, the particles align in the flow direction and organize to hexagonal structures in the 23-plane. The string phase is less sensitive to the particle size polydispersity compared to the equilibrium crystallization, i.e., a size polydispersity sufficient to prevent spontaneous crystallization is not enough to prevent string order formation.

Even in the string phase the stress is dominated by HIs, as the stress contribution from the excluded volume effects is only 0.6% of the total stress at $\mathrm{Pe}_\sigma = 595$ and 0.3% at $\mathrm{Pe}_\sigma = 1000$. The Péclet numbers with the string phase in Fig. 8.3 correspond to the location of the volume fraction "kink" in Fig. 8.1d. At other imposed pressures, the string phase formation is observed when $\bar{\Pi} \geq 20$ with volume fractions between

$\phi = 0.56$ and 0.58. Similar string phases are found in non-hydrodynamic Brownian dynamics simulations [34], in Accelerated Stokesian Dynamics simulations of non-Brownian monodisperse suspensions at $0.5 < \phi < 0.6$ [54], and in experiments [36, 37]. Their formation is commonly attributed to the the repulsive interparticle forces. It is unlikely the case here as the stress contribution from interparticle forces is low. Another interpretation is that HIs are localized and dominated by the pairwise lubrication interactions for very dense systems. The localized HIs may behave similarly to repulsive forces in non-hydrodynamic systems, and promote the string phase formation. On the other hand, at higher ϕ the limited available space cannot geometrically accommodate the string formation in suspensions.

Surprisingly, the string phase in Fig. 8.3 melts at higher Pe_σ. This is different from simulations without HIs, where the string order persists at higher Pe_σ [26]. A possible explanation is suspension dilation, as suspensions at lower ϕ are dominated by the long-range, non-pairwise-additive aspect of the HIs, which disrupts the string order formation. This explanation is also consistent with the observations in Fig. 8.2.

Beyond the melting of the string phase structures, the structural evolution of amorphous suspensions at $\bar{\Pi} = 50$ in Fig. 8.3 is similar to those at $\bar{\Pi} = 1.5$ in Fig. 8.2 with more pronounced structural features. For example, in the 12-plane, the particle depletion wake also approaches the velocity axis with increasing Pe_σ. In the 13-plane, the anisotropy in $g_{13}(\boldsymbol{r})$ at $\mathrm{Pe}_\sigma = 10^4$ is evident and clearly suggests a strong preference for the particles to align in the vorticity direction.

We have found that the vorticity alignment is present for all imposed pressures $\bar{\Pi}$ with high Pe_σ. Experimentally, the vorticity particle alignment was first discovered in sheared suspensions with strong confinement [7, 38], and was also recently found in experiments of sheared bulk suspensions [39, 40]. Numerical evidence, however, has been limited to simulations in confined systems [38, 41]. This work is the first numerical study for bulk suspensions that exhibits such alignment. Our results suggest that the vorticity particle alignment does not require confinement, high volume fractions, or Brownian motion. Therefore, it must originate from pairwise HIs. Indeed, the vorticity particle alignment is a consequence of the periodic particle trajectory in simple shear flow. Batchelor and Green [106] showed that the particle trajectories in simple shear flows contain a region of closed trajectories extending to infinity in the vorticity direction, and in this region, a particle pair undergoes periodic motion. As a result, when a particle enters the closed trajectory region of another particle, it is effectively locked in a periodic orbit until it encounters another particle.

Such hydrodynamic "trapping" increases the probability of particle presence in the vorticity direction, and therefore leads to the preferred vorticity alignment.

Quantitative details of the pair distribution function $g(\boldsymbol{r})$ significantly affect the suspension stress. In the $\mathrm{Pe}_{\dot{\gamma}} \gg 1$ limit, the dominant hydrodynamic stresslet $\boldsymbol{S}^{\mathrm{E}}$ can be approximated from the boundary-layer approximation [33, 107]

$$\boldsymbol{S}^{\mathrm{E}}_{\mathrm{b.l.}} \sim \eta'_{\infty}(\phi)\dot{\gamma}\phi^2 g^{\infty}(2;\phi)\times \int_{\hat{\boldsymbol{r}}\cdot\boldsymbol{E}\cdot\hat{\boldsymbol{r}}<0} \hat{\boldsymbol{r}}\hat{\boldsymbol{r}}(\hat{\boldsymbol{r}}\cdot\boldsymbol{E}\cdot\hat{\boldsymbol{r}})\bar{g}(\theta,\varphi)d\Omega, \tag{8.26}$$

where $\hat{\boldsymbol{r}}$ is the unit vector in the radial direction, η'_{∞} is the high-frequency dynamic shear viscosity, $g^{\infty}(2;\phi)$ is the pair distribution function outside the boundary layer, $\bar{g}(\theta,\varphi)$ is the $O(1)$ angular variation within the boundary layer, and Ω is the solid angle. From a radial-balance approximation, $\bar{g}(\theta,\varphi) \propto -\hat{\boldsymbol{r}}\cdot\boldsymbol{E}\cdot\hat{\boldsymbol{r}}$ [107]. In the $\mathrm{Pe}_{\dot{\gamma}} \ll 1$ limit, on the other hand, the deviatoric part of the Brownian stresslet $\boldsymbol{S}^{\mathrm{B}}$ is estimated as [33, 50]

$$n\left\langle \boldsymbol{S}^{\mathrm{B}}\right\rangle + \Pi^0\boldsymbol{I} = -\frac{27}{2\pi}\eta_0\dot{\gamma}\phi^2\frac{g^0(2,\phi)}{\hat{d}(\phi)}\times \int \hat{\boldsymbol{r}}\hat{\boldsymbol{r}}\,\hat{f}(2;\theta,\varphi)d\Omega, \tag{8.27}$$

where Π^0 is the equilibrium osmotic pressure, $g^0(2,\phi)$ is the equilibrium contact value of the pair distribution function, $\hat{d}(\phi)$ is a characteristic diffusion scale relative to the single particle value, and $\hat{f}(\boldsymbol{r})$ is the distortion of the equilibrium pair distribution function $g(\boldsymbol{r})/g^0(\boldsymbol{r}) = 1+[\mathrm{Pe}_{\dot{\gamma}}/\hat{d}(\phi)]\hat{f}(\boldsymbol{r})$. Eq. (8.26) and (8.27) are derived for monodisperse suspensions, and are helpful for formulating scaling arguments to collapse the rheology results in the liquid-like regime [33, 54]. In addition, they also reveal that the most significant structural contributions are from the extensional and the compressional axes indicated in Fig. 8.2 and 8.3. Furthermore, Eq. (8.26) and (8.27) show that both the extensional and the compressional quadrant contribute positively to η^{B} and η^{E} in their respective regimes.

Fig. 8.4 presents the peak values of the of the pair distribution on the compressional axis, $\max(g_{\mathrm{comp}})$ (filled symbols), and on the extensional axis, $\max(g_{\mathrm{ext}})$ (open symbols), as functions of Pe_{σ} at $\bar{\Pi} = 1.5$ and $\bar{\Pi} = 50$. The insets of Fig. 8.4 also show $g_{\mathrm{comp}}(r)$ (solid lines) and $g_{\mathrm{ext}}(r)$ (dashed lines) as selected Pe_{σ}. Here, the data at different Pe_{σ} are shifted for clarity. For liquid-like suspensions at $\bar{\Pi} = 1.5$ in Fig. 8.4a, at $\mathrm{Pe}_{\sigma} = 0.2$, $\max(g_{\mathrm{comp}})$ and $\max(g_{\mathrm{ext}})$ are almost identical, consistent

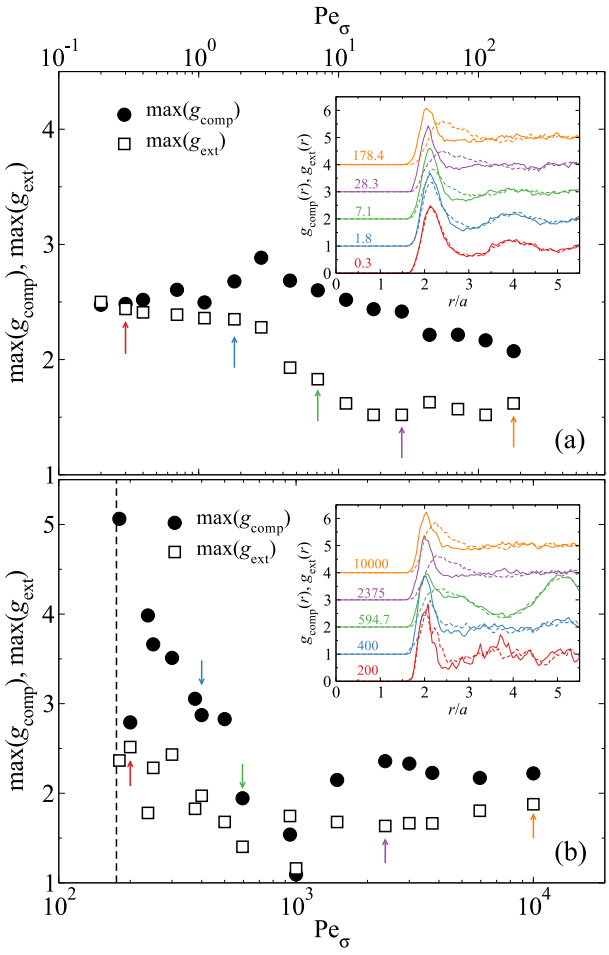

Figure 8.4: (Color online) The maximum value of the pair distribution functions on the compressional and the extensional axes, $\max(g_{\text{comp}})$ (filled symbols) and $\max(g_{\text{ext}})$ (open symbols), respectively, as functions of Pe_σ at (a) $\bar{\Pi} = 1.5$ and (b) $\bar{\Pi} = 50$. The insets show $g_{\text{comp}}(r)$ (solid lines) and $g_{\text{ext}}(r)$ (dashed lines), obtained from the equatorial slices of $g(\boldsymbol{r})$ in the 12-plane with a width of $0.7a$, at selected Pe_σ annotated by arrows in the main figure. The $g_{\text{comp}}(r)$ and $g_{\text{ext}}(r)$ results are shifted for clarity. In (b) the estimated flow-arrest transition Pe_σ is shown in the vertical dashed line.

with the almost isotropic suspension structure in Fig. 8.2. With increasing Pe_σ, $\max(g_{\text{comp}})$ first increases, reaches a maximum at $\text{Pe}_\sigma = 2.8$, and then decreases. On the other hand, $\max(g_{\text{ext}})$ first decreases slowly when $\text{Pe}_\sigma < 2.8$, and reduces more quickly with respect to Pe_σ until $\text{Pe}_\sigma = 28.3$, where $\max(g_{\text{ext}})$ grows mildly with Pe_σ again. These rich structural features arise from the HIs in the constant stress and pressure rheology. The inset of Fig. 8.4a provides further insights to the structural changes. Increasing Pe_σ reduces the width of the first peak of $g_{\text{comp}}(r)$ and

flattens the undulation of $g_{\text{comp}}(r)$ beyond the first peak, suggesting a compression of neighboring particles and the dominance of pair interactions in this direction with high imposed stresses. On the other hand, increasing Pe_σ shifts the location of the $g_{\text{ext}}(r)$ maximum away from the particle surface, reduces the undulations beyond the first peak, and also qualitatively changes the shape of $g_{\text{ext}}(r)$, e.g., $g_{\text{ext}}(r)$ at $\text{Pe}_\sigma = 28.3$ is notably different from the near-equilibrium structure at $\text{Pe}_\sigma = 0.3$. Comparing to Fig. 8.2, the changes in $g_{\text{ext}}(r)$ is associated with the development of the particle depletion wake in the extensional quadrant.

The structural features in the compressional and the extensional axes at $\bar{\Pi} = 50$ are presented in Fig. 8.4b. Despite slightly scattered data, $\max(g_{\text{comp}})$ and $\max(g_{\text{ext}})$ are different from the onset of flow near the flow-arrest transition, suggesting that the flow of glassy suspensions is inherently far from equilibrium. With increasing Pe_σ up to $\text{Pe}_\sigma = 1000$, both $\max(g_{\text{comp}})$ and $\max(g_{\text{ext}})$ decrease, and their difference is also diminishing. In fact, $\max(g_{\text{comp}})$ and $\max(g_{\text{ext}})$ become almost identical with the string phase formation. After the dissolution of the string phase at $\text{Pe}_\sigma > 10^3$, $\max(g_{\text{comp}})$ first increases and then decreases, and $\max(g_{\text{ext}})$ increases mildly with growing Pe_σ, similarly to the high Pe_σ behaviors at $\bar{\Pi} = 1.5$. In the inset of Fig. 8.4b, $g_{\text{comp}}(r)$ and $g_{\text{ext}}(r)$ at $\text{Pe}_\sigma = 200$ and 400 exhibit fluctuations due to the slow suspension structural evolution. At $\text{Pe}_\sigma = 594.7$, the formation of string order phase qualitatively changes $g_{\text{comp}}(r)$ and $g_{\text{ext}}(r)$ from amorphous suspensions at other Pe_σ, including the formation of significant undulations beyond the first peak. The structural features of $g_{\text{comp}}(r)$ and $g_{\text{ext}}(r)$ at $\text{Pe}_\sigma = 2375$ and 10^4 are similar to those at $\text{Pe}_\sigma = 28.3$ and 178.4 at $\bar{\Pi} = 1.5$ in Fig. 8.4a.

Dynamics: long-time self-diffusivity

The diffusive dynamics of the suspension are characterized by the long-time self-diffusivities in the velocity gradient direction $d^s_{\infty,22}$ and the vorticity direction $d^s_{\infty,33}$. The diffusivity in direction k is calculated as

$$d^s_{\infty,kk} = \frac{1}{2} \lim_{t\to\infty} \frac{\mathrm{d}\left\langle \Delta x_k^2 \right\rangle}{\mathrm{d}t}, \tag{8.28}$$

where $\left\langle \Delta x_k^2 \right\rangle$ is the particle mean-square displacement computed from all available data.

Fig. 8.5a present $d^s_{\infty,33}$ as functions of Pe_σ at $\bar{\Pi} = 1.5$. At this imposed pressure, the zero-shear diffusivity is finite, and $d^s_{\infty,33}$ increases with Pe_σ. The inset of Fig. 8.5 shows the mean square displacement $\left\langle \Delta x_3^2 \right\rangle$ as functions of the dimensionless time

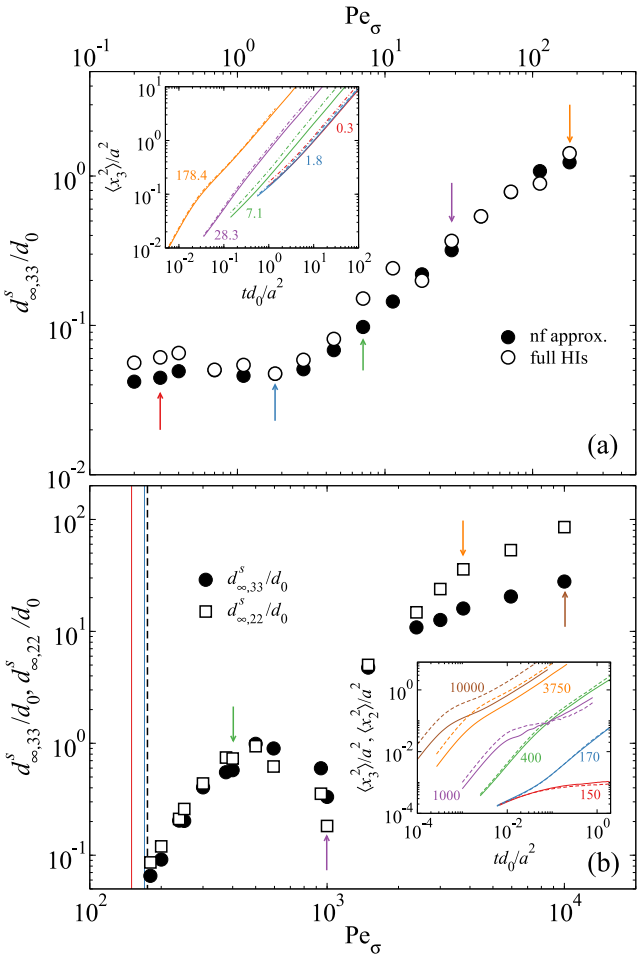

Figure 8.5: (Color online) Long-time self-diffusivity in the vorticity (3-) and the velocity gradient (2-) direction, $d^s_{\infty,33}/d_0$ and $d^s_{\infty,22}/d_0$, respectively, at (a) $\bar{\Pi} = 1.5$ and (b) $\bar{\Pi} = 50$. (a): $d^s_{\infty,33}/d_0$ computed with full HIs (open symbols) and with the near-field Brownian approximation (filled symbols). Inset: the time trace of the mean-square displacement in the 3-direction, $\left\langle \Delta x_3^2 \right\rangle$ at different Pe_σ. The solid lines are from the near-field Brownian approximation and the dash-dotted lines are from full calculations. (b): $d^s_{\infty,33}/d_0$ (filled circles) and $d^s_{\infty,22}/d_0$ (open squares) from near-field Brownian approximation as functions of Pe_σ. Inset: the time trace of the mean-square displacement in the 3-direction $\left\langle \Delta x_3^2 \right\rangle$ (solid lines) and the 2-direction $\left\langle \Delta x_2^2 \right\rangle$ (dashed lines) at different Pe_σ.

ta^2/d_0: at small Pe_σ, $\left\langle \Delta x_3^2 \right\rangle$ is observed to first grow sublinearly, and then linearly with time. Since the particle dynamics in the $\mathrm{Pe}_\sigma \ll 1$ limit are dominated by Brownian motion, $\left\langle \Delta x_3^2 \right\rangle$ is expected to grow linearly with time at a smaller time scale not captured in the figure, and its rate of growth characterizes the translational short-time self-diffusivity d^t_s. With $\mathrm{Pe}_\sigma \gg 1$, e.g. $\mathrm{Pe}_\sigma = 178.4$, $\left\langle \Delta x_3^2 \right\rangle$ grows

linearly with time at long times, but proportional to t^2 when $td_0/a^2 < 0.02$. This is because in the short-time limit, the particle dynamics are dominated by the flow, i.e., $\left\langle \Delta x^2 \right\rangle \sim (\dot{\gamma} t)^2$. However, at larger time scale, the extensive interaction with neighboring particles restores the diffusive motion. Moreover, Fig. 8.5a also compares the results from full hydrodynamic computations and from the near-field Brownian approximation. Their agreement is satisfactory despite small quantitative differences.

The suspension dynamics at $\bar{\Pi} = 50$ are shown in Fig. 8.5b, where both $d^s_{\infty,33}$ and $d^s_{\infty,22}$ are presented in the main figure and $\left\langle \Delta x_2^2 \right\rangle$ and $\left\langle \Delta x_3^2 \right\rangle$ in the inset. There are several noteworthy features. First, when the imposed stress is much smaller than the yield stress, e.g. at $\mathrm{Pe}_\sigma = 150$, the suspension arrests and the long-time self-diffusivities vanish. At this Pe_σ, the mean square displacement does not grow linearly with time, but rather reaches a constant value characterizing the size of the confining cage. Close to the flow-arrest transition, e.g., at $\mathrm{Pe}_\sigma = 170$, the suspension becomes activated and there is a small but finite diffusivity. Unlike the liquid-like suspensions at $\bar{\Pi} = 1.5$ in Fig. 8.5a, the suspensions do not exhibit a zero-shear diffusivity. As the imposed stress exceeds the yield stress, the diffusivities grow with Pe_σ, and exhibit little anisotropy, i.e., $d^s_{\infty,33} \approx d^s_{\infty,22}$. At higher Pe_σ, however, the diffusivities decrease due to the string order formation seen in Fig. 8.3. The qualitative influences of structural formation in the suspension dynamics are also evidenced by the distinct $\left\langle \Delta x_2^2 \right\rangle$ and $\left\langle \Delta x_3^2 \right\rangle$ at $\mathrm{Pe}_\sigma = 10^3$ in Fig. 8.5b inset. Moreover, with the dissolution of the string order phase at higher Pe_σ, $d^s_{\infty,22}$ becomes much higher than $d^s_{\infty,33}$, suggesting anisotropy in the suspension dynamics. From the inset, the particles move more easily in the 2-direction due to the enhanced velocity fluctuations in the non-Brownian limit [43].

8.4 A granular perspective on colloidal rheology

Here we examine the constant stress and pressure rheology of dense colloidal suspensions using a granular perspective. The results with string order formation are not included because, as is shown in Sec. 8.3, the string order phase introduces qualitatively different suspension behaviors.

Mechanical responses

Fig. 8.6 presents the shear viscosity η_s/η_0, the volume fraction ϕ, and the *macroscopic* friction coefficient $\mu = \sigma/\Pi$ as functions of the viscous number $I_v = \dot{\gamma}\eta_0/\Pi$ defined in Eq. (8.3) over a wide range of imposed pressures $\bar{\Pi}$ from the constant

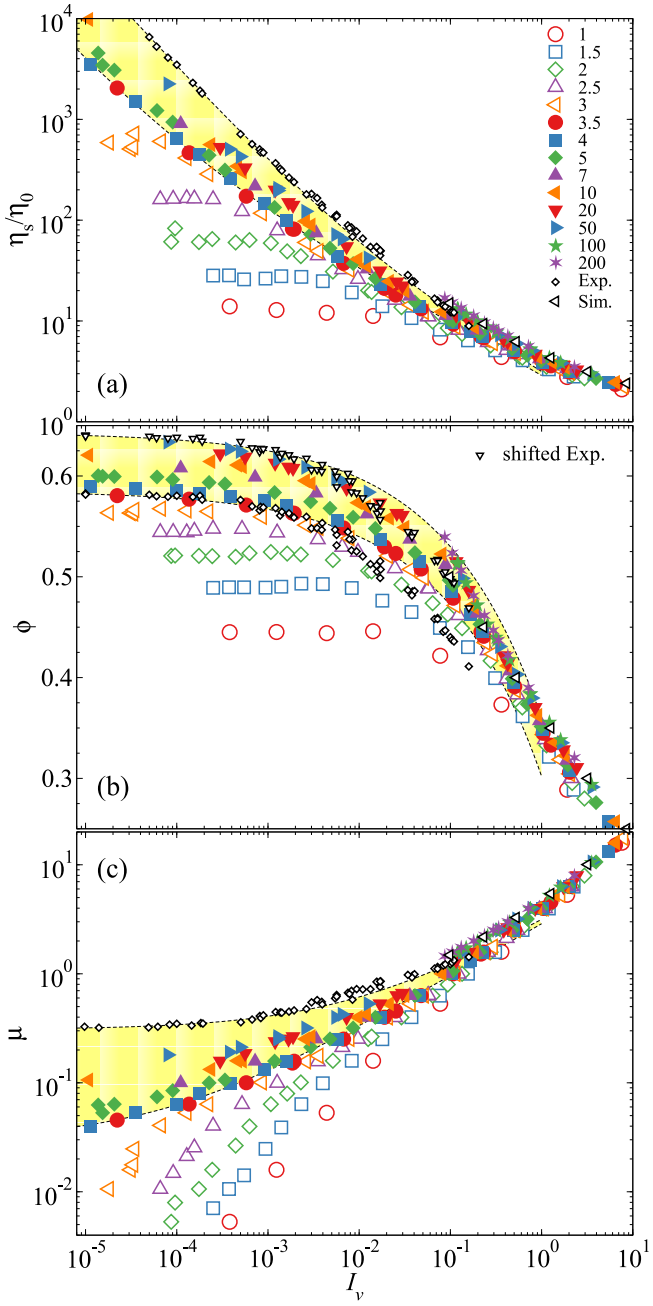

Figure 8.6: (Color online) The suspension shear viscosity η_s/η_0 (a), the volume fraction ϕ (b), and the *macroscopic* friction coefficient $\mu = \sigma/\Pi$ as functions of the viscous number $I_v = \dot{\gamma}\eta_0/\Pi$ with different imposed pressures $\bar{\Pi}$. Also presented are the non-Brownian results from experiments [24] (black open diamonds) and Accelerated Stokesian Dynamics (ASD) simulations at fixed strain rate $\dot{\gamma}$ and volume fraction ϕ [54] (black open left triangles). The shaded area bounded by dashed lines are from the rheological model outlining the boundary of glassy suspensions. The experimental results shifted upwards to ϕ_{SAP} are also presented in (b) (black open down triangles).

stress and pressure simulations. In Fig. 8.6 the liquid-like suspensions, which do not develop a yield stress, are shown as open symbols, and glassy suspensions, which exhibit flow-arrest transitions, are shown as filled symbols. Using I_v highlights the importance of pressure on the suspension rheology. Consistent with Fig. 8.1, with constant imposed pressure, η_s/η_0 and ϕ decrease, and μ increases with increasing I_v. In the limit $I_v \to \infty$, the shear viscosity η_s approaches the solvent viscosity η_0, the volume fraction ϕ asymptotes zero, and the friction coefficient μ grows without bound due to suspension dilation. Fig. 8.6 is similar to the results without HIs [25, 26] with quantitative differences. In addition, for comparison Fig. 8.6 also present results from the experiments of Boyer et al. [24] and the Accelerated Stokesian Dynamics (ASD) simulations of Sierou and Brady [54] on non-Brownian suspensions.

Fig. 8.6a shows the suspension shear viscosity η_s/η_0. Liquid-like suspensions occur at low imposed pressures $\bar{\Pi} < 3.5$, and they exhibit a zero-shear viscosity in the $I_v \to 0$ limit, which grows with increasing $\bar{\Pi}$. At higher confining pressures, $\bar{\Pi} \geq 3.5$, the zero-shear viscosity disappears as the suspension develops yield stresses. When $I_v \gg 1$, the data collapse towards the solvent viscosity η_0 at all imposed pressures due to suspension dilation. For small I_v, the differences among the isobaric η_s decrease with increasing $\bar{\Pi}$. As $\bar{\Pi} \to \infty$, a non-Brownian limit is expected to emerge. However, the highest pressure with $I_v < 0.1$ in our simulations is $\bar{\Pi} = 50$. At higher imposed pressure, reaching a low I_v without significant stress contributions from the interparticle forces is computationally difficult. Reducing the dimensionless time step $\Delta\tau$ from 0.01 to 0.0025 only marginally reduces the viscous number I_v where the interparticle force stress contribution is less than 1%. Therefore, despite an evident tendency, the imposed pressures $\bar{\Pi}$ in the simulations is not high enough to achieve the limiting non-Brownian viscosity.

In Fig. 8.6a the suspension viscosity in the non-Brownian limit is established from the non-Brownian experiments [24] and ASD simulations [54], shown in open diamonds and triangles in black, respectively. The experiments and simulations complement the entire I_v range with $I_v \lesssim 0.1$ from the experiments and $I_v \gtrsim 0.1$ from the simulations. At $I_v \approx 0.1$, the experimental and the numerical results overlap and agree well, showing consistent non-Brownian suspension behaviors. The small difference between the non-Brownian experiments and simulations may arise from different interparticle forces [54]. The suspension viscosity from the constant stress and pressure simulation agree well with the non-Brownian simulation

data for $I_v \gtrsim 0.1$. At $I_v < 0.1$, the experiments suggest that the viscosities at $\bar{\Pi} = 50$ have not yet reached the non-Brownian limit.

Fig. 8.6b presents the volume fraction ϕ as a function of I_v at various imposed pressures. Consistent with Fig. 8.1, the results show that, for a given I_v, increasing the imposed pressure compresses the suspension, and at fixed pressure, increasing I_v dilates the suspension. For $I_v \ll 1$, the volume fraction asymptotes a value corresponding to the $I_v \to 0$ limit. When $I_v > 1$, the volume fractions collapse to a non-Brownian limiting behavior with $\phi < 0.35$ for all imposed pressures $\bar{\Pi}$. With $I_v < 1$, only a tendency for data collapse is found with $\bar{\Pi} \geq 10$. Similarly to Fig. 8.6a, our imposed pressure $\bar{\Pi}$ is not high enough for the non-Brownian limiting behavior to be reached in the double limit $I_v \to 0$ and $\bar{\Pi} \to \infty$.

The non-Brownian results from earlier simulations and experiments are also presented in Fig. 8.6b. At the common I_v range covered by both the experiments and the simulations, the volume fraction results are inconsistent. At $I_v \approx 0.1$, ϕ from the ASD simulations [54] are significantly higher than the experimental data, due to the significantly lower maximum volume fraction $\phi_c \approx 0.585$ in the experiments. Simply shifting the experimental ϕ upwards by an amount of $(\phi_{\text{SAP}} - \phi_c)$ restores the consistency in the non-Brownian results. In Fig. 8.6b, the shifted experimental data are shown in down triangles. The SAP volume fraction ϕ_{SAP} is independently determined from the constant stress and pressure simulation data without the knowledge of earlier non-Brownian results, and is described in later. When $I_v > 0.1$, the shifted non-Brownian ϕ is slightly lower than the collapsed data from the constant stress and pressure simulations, most likely due to the particle size polydispersity in the latter. On the other hand, in the $I_v \ll 1$ limit, the volume fraction behaviors at $\bar{\Pi} = 50$ is close to the shifted non-Brownian results.

Fig. 8.6c presents the *macroscopic* friction coefficient μ as a function of I_v. For liquid-like suspensions with $\bar{\Pi} < 3.5$, μ increases linearly with I_v when $I_v \ll 1$ because the ratio $\mu/I_v = \eta_s/\eta_0$, and the initial linear increase in μ characterizes the suspension's zero-shear viscosity. For glassy suspensions with $\bar{\Pi} \geq 3.5$, the suspensions develop a yield stress, as μ asymptotes a constant, finite value in the limit $I_v \to 0$. Similar to Fig. 8.6a and 8.6b, the friction coefficient data collapse for all imposed pressures when $I_v \gg 1$, and a tendency of data collapse is evident with $\bar{\Pi} \geq 10$ when $I_v \ll 1$. The results from earlier non-Brownian experiments and ASD simulations are also presented in Fig. 8.6c. The non-Brownian experiments and simulations agree for the overlapping viscous numbers near $I_v \approx 0.1$, suggesting

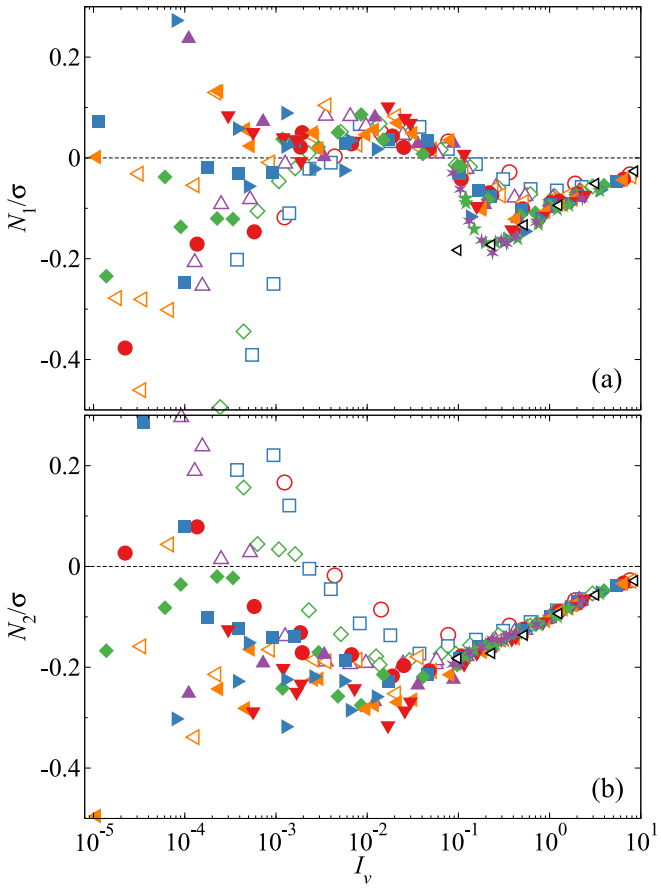

Figure 8.7: (Color online) The first and the second normal stress differences scaled with the shear stress, N_1/σ (a) and N_2/σ (b), as functions of the viscous number I_v at various imposed pressures $\bar{\Pi}$. Also presented are the non-Brownian ASD simulation results [54]. The legends are identical to those of Fig. 8.6.

a consistent behavior similar to the consistent viscosity in Fig. 8.6a. The non-Brownian friction coefficient μ with $I_v \gtrsim 0.1$ agree well with the collapsed constant stress and pressure simulation results. When $I_v \lesssim 0.1$, however, the experiments of Boyer et al. [24] show a higher limiting friction coefficient compared to the limiting μ at $\bar{\Pi} = 50$. Our results suggest that, the expected μ from simulations in the $\bar{\Pi} \to \infty$ and $I_v \to 0$ limits should be consistent with the non-Brownian experimental results here.

The first and the second normal stress differences, N_1 and N_2, are computed from the total stress $\langle \boldsymbol{\Sigma} \rangle$ as,

$$N_1 = \langle \Sigma_{11} \rangle - \langle \Sigma_{22} \rangle , \tag{8.29}$$

$$N_2 = \langle \Sigma_{22} \rangle - \langle \Sigma_{33} \rangle . \tag{8.30}$$

Fig. 8.7a and 8.7b respectively present the scaled normal stress differences, N_1/σ and N_2/σ, as functions of the viscous number I_v at different imposed pressures $\bar{\Pi}$. In the high I_v regime ($I_v > 0.5$ for N_1 and $I_v > 0.1$ for N_2), both N_1 and N_2 are negative, and collapse to non-Brownian limiting behaviors at different $\bar{\Pi}$. The negative N_1 is the signature of HIs in the suspensions, because, to separate a particle pair, the HIs pull the pair together, while the interparticle forces push it apart. The former lead to negative N_1, while the latter to positive [33, 54, 56]. The magnitude of N_1/σ and N_2/σ decreases with increasing I_v due to suspension dilation. This is in contrast to the fixed volume rheology where N_1 and N_2 asymptote high-shear limiting values [33, 56]. The non-Brownian ASD simulation results [54] are also presented in Fig. 8.7, and they agree well with the collapsed constant stress and pressure simulations, except for N_1 at $I_v = 0.1$. The first normal stress difference N_1 near $I_v = 0.1$ are close to zero for all imposed pressures, and with $I_v > 0.1$, they first reach a negative minimum before increasing again. The non-Brownian simulation results only show increase in N_1 with growing I_v, as fluctuations in ϕ about its average value for $I_v \approx 0.1$ may reduce $|N_1|$ compared to the corresponding fixed ϕ simulations.

In the low shear limit, dilute theories [105, 108] predict that N_1 increases and N_2 decreases from zero in a fashion proportional $\dot{\gamma}^2$. The simulation results in Fig. 8.7 do not reveal such behaviors, suggesting that I_v is not sufficiently low. On the other hand, N_1 and N_2 behave distinctly in the low I_v regime. In Fig. 8.7a, N_1 is largely negative when $I_v < 10^{-3}$. The general trend is that, with increasing $\bar{\Pi}$, N_1 at $I_v < 10^{-5}$ shifts from negative to positive. In the range $10^{-3} < I_v < 0.1$, N_1 becomes loosely collapsed. It first becomes slightly positive and decreases after reaching a maximum. The second normal stress difference N_2 in Fig. 8.7b reduces from the lower I_v limit and reaches a local minimum before collapsing to the high I_v behaviors. The N_2 values at $I_v < 10^{-5}$ decrease from positive to negative with increasing $\bar{\Pi}$, and become increasingly noisy. The low I_v behaviors in Fig. 8.7a and 8.7b demonstrate the complex interplay of between Brownian motion and HIs in polydisperse suspensions.

Structural peaks

The peak values of pair distribution function along the compressional and the extensional axes, $\max(g_{\text{comp}})$ and $\max(g_{\text{ext}})$, are key suspension structural features. As discussed in Sec. 8.3, they are closely related to the suspension rheology, and are strongly affected by the particle Brownian motion and HIs. Fig. 8.8 presents

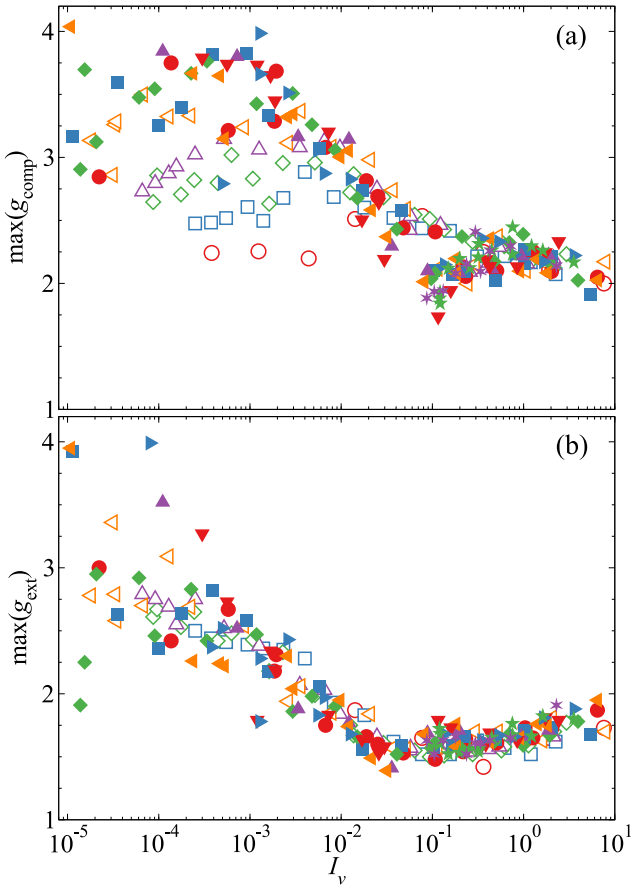

Figure 8.8: (Color online) The peak values of the pair distribution function along the compressional and the extensional axes, max(g_{comp}) (a) and max(g_{ext}) (b), as functions of the viscous number I_v at various imposed pressures $\bar{\Pi}$. The legends are identical to those of Fig. 8.6.

max(g_{comp}) and max(g_{ext}) as functions of the viscous number I_v over different imposed pressures $\bar{\Pi}$.

Fig. 8.8a focuses on the peak value of the pair distribution function along compressional axis, max(g_{comp}). For liquid-like suspensions with $\bar{\Pi} < 3.5$, max(g_{comp}) first increases and then decreases with increasing I_v. The decrease of max(g_{comp}) at different $\bar{\Pi}$ largely collapse. With increasing $\bar{\Pi}$ the peak value max(g_{comp}) in the equilibrium limit also grows, and joins the collapsed max(g_{comp}) decrease at a smaller I_v. For glassy suspensions with $\bar{\Pi} \geq 3.5$, max(g_{comp}) also collapses at small I_v: the initial increase takes place at $I_v < 10^{-4}$, followed by a plateau until $I_v \approx 10^{-3}$. Further increase in I_v lead to decrease in max(g_{comp}). With $I_v \gtrsim 0.1$, max(g_{comp}) discontinuously drops to max(g_{comp}) ≈ 2, reaches a maximum, and decreases again

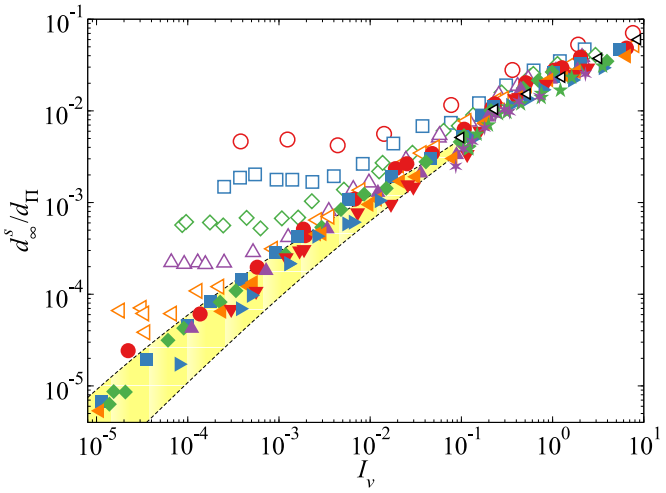

Figure 8.9: (Color online) The long-time self-diffusivity in the vorticity direction scaled with the pressure diffusion scale d^s_∞/d_Π, where $d_\Pi = a^2\Pi/\eta_0$, as functions of the viscous number I_v at various imposed pressures $\bar{\Pi}$. Also presented are the non-Brownian ASD simulation results [43, 54]. The yellow shaded region bounded by dashed liens are predictions from Eq. (8.43). The legends are identical to those of Fig. 8.6.

along with the lower $\bar{\Pi}$ results. The discontinuous behavior of $\max(g_{\text{comp}})$ is likely associated with the string phase structures in Fig. 8.3.

Fig. 8.8b shows the changes of $\max(g_{\text{ext}})$ with respect to I_v at various I_v. In the extensional axis, the peak values of g_{ext} collapse better compared to $\max(g_{\text{comp}})$ in Fig. 8.8a: with increasing I_v, $\max(g_{\text{ext}})$ first decreases, reaching a minimum at $I_v \approx 0.1$, and then increases slightly. The data in the $I_v \to 0$ limit are somewhat scattered, but unlike $\max(g_{\text{comp}})$, they do not show different low I_v limiting values at different $\bar{\Pi}$. Moreover, the range of I_v corresponding to $\max(g_{\text{ext}})$ increases is also the I_v range where $\max(g_{\text{comp}})$ becomes discontinuous, suggesting that they are caused by the same mechanism, possibly due to the stronger HIs among particles. Fig. 8.8 highlights the importance of the compressional quadrant on the structural contributions to the suspension rheology in the low I_v limit.

Long-time self-diffusivity

We characterize the particle diffusive dynamics using the long-time self-diffusivity in the vorticity direction, $d^s_{\infty,33}$, and for simplicity refer to it as d^s_∞ in the following discussion. Usually, the diffusion of Brownian suspensions is compared with the single-particle Stokes-Einstein-Sutherland diffusivity d_0, as is the case of Fig. 8.5.

However, for strongly driven suspensions far from equilibrium, a different diffusion scale may necessary as thermal fluctuations may be irrelevant for the suspension dynamics. For the constant stress and pressure simulations in this work, we choose the pressure diffusion scale,

$$d_\Pi = a^2\Pi/\eta_0, \tag{8.31}$$

for the characterization of the diffusivity d^s_∞.

Fig. 8.9 presents the scaled diffusivity d^s_∞/d_Π as functions of the viscous number for different $\bar{\Pi}$, with liquid-like suspensions ($\bar{\Pi} < 3.5$) in open symbols and glassy suspensions ($\bar{\Pi} \geq 3.5$) in filled symbols. For liquid-like suspensions, d^s_∞/d_Π increases with I_v from a plateau corresponding to the equilibrium at-rest value. Increasing $\bar{\Pi}$ reduces the at-rest diffusivity d^s_∞/d_Π, as both the equilibrium self-diffusivity decreases with the volume fraction ϕ and the pressure increases with ϕ. In addition, increasing $\bar{\Pi}$ also reduces the viscous number I_v where d^s_∞/d_Π departs from the at-rest values, e.g., at $\bar{\Pi} = 1$, d^s_∞ departs the plateau at $I_v \approx 10^{-2}$, and at $\bar{\Pi} = 2.0$, the departure viscous number is $I_v \approx 10^{-3}$. With $I_v > 0.1$, the difference in d^s_∞/d_Π between different $\bar{\Pi}$ reduces significantly.

For glassy suspensions, d^s_∞/d_Π does not show a plateau and always increases with increasing I_v. The lack of a plateau suggests that the at-rest diffusion vanishes, i.e., as $d^s_\infty/d_\Pi \to 0$ as $I_v \to 0$. Therefore, in the glassy regime, particles are frozen by their neighbors at $\dot{\gamma} = 0$, and the diffusion process is restored with flow ($\dot{\gamma} \neq 0$). The pressure scaled diffusivity d^s_∞/d_Π for glassy suspensions is lower than its liquid-like counterpart and decreases with further pressure increase. In the non-Brownian high-pressure limit $\Pi \to \infty$, d^s_∞/d_Π collapses to a jamming limit as evidenced by the data collapse trend in Fig. 8.9. In this limit, d^s_∞/d_Π remains finite despite diverging pressure, and grows with I_v. Fig. 8.9 highlights the importance of pressure in suspension dynamics, an frequently overlooked aspect in studies at lower Π or ϕ. Note that Eq. (8.31) is similar to the single-particle d_0 by replacing the thermal energy scale $k_\mathrm{B}T$ with a pressure energy scale $a^3\Pi$. The collapse of d^s_∞/d_Π in the high pressure limit suggests that the pressure may be considered a measure of the internal fluctuations in the system, which are explored in Sec. 8.5.

Fig. 8.9 also presents the non-Brownian ASD simulation results [43, 54] (in black open left triangles) for comparison, as they are the only rheology studies with appropriate normal stress and diffusion characterizations. The non-Brownian results agree well with the high pressure results with $I_v > 0.1$, providing an independent validation for the constant stress and pressure simulations. The shaded region

bounded by dashed lines in Fig. 8.9 is the glassy regime predicted by the model presented Sec. 8.4 together with the universal collapse found in Sec. 8.5. The non-Brownian limit from the model, shown as the lower dashed line in Fig. 8.9, can only achieved with simulations at higher imposed pressures.

A model for glassy rheology

Fig. 8.6 shows that the rheological behavior of glassy suspensions ($\bar{\Pi} \geq 3.5$ in filled symbols) is similar to the non-Brownian limiting behavior. For example, all glassy suspensions exhibit a viscosity divergence and the emergence of yield stress as $I_v \to 0$. Physically, as the suspensions become glassy with sufficiently high imposed pressure, its at-rest dynamics become extremely slow and its flow behavior becomes dominated by the external forcing. In other words, if we characterize the at-rest dynamics of suspensions using a diffusivity d_T, in the glassy state, the particles are effectively locked by their neighbors, and therefore d_T/d_0 vanishes. Therefore, as soon as the suspension begins to flow, the effective Péclet number $\mathrm{Pe}_T = \dot{\gamma}a^2/d_T \gg 1$ as long as $\dot{\gamma}$ is finite. Consequently, it is clear that the non-Brownian dynamics dominate the behavior of glassy suspensions. This is one of the principle conclusions of our earlier work [25].

The rheology of non-Brownian suspensions beyond the flow-arrest transition can be characterized by the departure of ϕ and μ from their arrest values,

$$\phi = \phi_m - \delta\phi \quad \text{and} \quad \mu = \mu_m + \delta\mu, \tag{8.32}$$

where μ_m and ϕ_m are the limiting arrest friction coefficient and volume fraction, and $\delta\mu$ and $\delta\phi$ characterize how the suspension departures from the arrested state. For non-Brownian systems, $\delta\mu$ and $\delta\phi$ depends only on the viscous number, and assuming a power law,

$$\delta\phi = K_\phi I_v^{\alpha_\phi} \quad \text{and} \quad \delta\mu = K_\mu I_v^{\alpha_\mu}, \tag{8.33}$$

where K_ϕ, α_ϕ, K_μ, and α_μ are constants. Eq. (8.33) describes a wide range of experiments and simulations of non-Brownian systems, and is also suggested from theoretical investigations [68, 69].

We characterize the glassy rheology for $I_v < 1$ in Fig. 8.6 using Eq. (8.32) and (8.33). Since the physics of jamming dominates the glassy suspension behavior, we speculate that the power law relations in Eq. (8.33) are unaffected by thermal fluctuations and are independent of the imposed pressure $\bar{\Pi}$. Meanwhile, the arrest

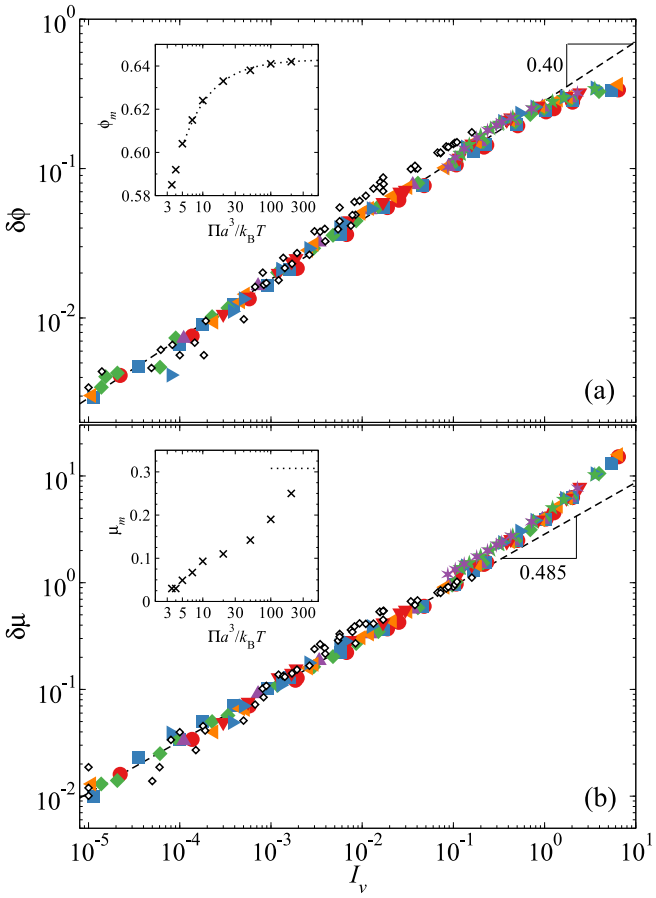

Figure 8.10: (Color online) The incremental volume fraction $\delta\phi = \phi_m - \phi$ (a) and friction coefficient $\delta\mu = \mu - \mu_m$ (b) as functions of the viscous number I_v for glassy suspensions with $\bar{\Pi} \geq 3.5$. The dashed lines in the main figures show Eq. (8.33) with parameters in Table 8.1. The insets show the limiting volume fraction ϕ_m (a) and the limiting friction coefficient μ_m (b) as functions of the imposed pressure $\bar{\Pi}$. The dashed line in the inset of (a) shows Eq. (8.34), and the dashed line in the inset of (b) is the non-Brownian μ_{SAP}. Also presented are the non-Brownian experimental results [24] in open black diamonds. The legends are identical to those in Fig. 8.6.

volume fraction ϕ_m and friction coefficient μ_m change with the imposed pressure. We find the optimal parameters that best describe the results in Fig. 8.6 using non-linear regression. Note that the non-Brownian limiting results from experiments [24] and simulations [54] are *not* considered in the regression process, and can be used as an independent check.

Fig. 8.10 presents $\delta\phi$ and $\delta\mu$ as functions of I_v for glassy suspensions with $\bar{\Pi} \geq 3.5$. The parameters for Eq. (8.33) from the regression analysis are shown in the first two columns of Table 8.1. Here, the volume fraction exponent $\alpha_\phi = 0.40$ is close to

the theoretical prediction of 0.35 [68], and is consistent with simulations of inertial systems [109] and non-Brownian viscous systems without HIs in the zero-pressure limit [62], where both studies have found $\alpha_\phi = 0.39$. The friction coefficient exponent $\alpha_\mu = 0.485$ is close to the non-Brownian experiments of Boyer et al. [24] which have a value of 0.5. The fitted ϕ_m and μ_m as functions of the imposed pressure $\bar{\Pi}$ are presented in the corresponding insets. The excellent data collapse suggests that Eq. (8.33) adequately describes the glassy suspension behavior for imposed pressures $\bar{\Pi}$ from 3.5 to 200. Also presented in Fig. 8.10 are the non-Brownian experimental results [24]. The simulation results agree with the experiment when the experimental critical friction coefficient μ_c is shifted from 0.32 to 0.308 with the original critical volume fraction $\phi_c = 0.585$. Here, Eq. (8.33) also satisfactorily describes the non-Brownian experimental data, which are not considered in the regression analysis. Fig. 8.10 shows that Eq. (8.33) with a single set of parameters describes glassy suspension behavior for $\bar{\Pi} \geq 3.5$ including the non-Brownian limit. It confirms our assertion that the dynamics of glassy dynamics are dominated by jamming, and that thermal fluctuations only affect the location of the flow-arrest transitions.

The insets of Fig. 8.10 show the locations of the flow-arrest transitions, (μ_m, ϕ_m), at different imposed pressures $\bar{\Pi} \geq 3.5$. In constant stress and pressure rheology, the smallest pressure where the suspension begins to exhibit flow-arrest transitions is called the glass transition pressure $\bar{\Pi}_G$, and in this work $\bar{\Pi}_G = 3.5$, with the corresponding glassy arrest location $(\mu_G, \phi_G) = (0.03, 0.585)$ from Fig. 8.10. The volume fraction ϕ_G is consistent with the hard-sphere colloidal glass transition, which is often marked by the divergence of the viscosity or the relaxation time [18, 22]. The finite μ_G at the glass transition suggests the sudden appearance of a yield stress, consistent with mode-coupling theory predictions [110]. To find the flow-arrest transition location in the $\bar{\Pi} \to \infty$ limit—the SAP—it is necessary to consider the non-Brownian experimental results [24], as the maximum imposed pressures for $I_v \ll 1$ are not sufficiently high. From the excellent collapse of $\delta\mu$ in Fig. 8.10b, we adopt the adjusted experimental limiting friction coefficient $\mu_c = 0.308 = \mu_{\text{SAP}}$. Determining ϕ_{SAP} is more subtle, because, as is shown in Fig. 8.6b, the original experimental ϕ is incompatible with the numerical results. Here, we found that the arrest volume fractions $\phi_m > 0.60$ with $\bar{\Pi} \leq 50$ satisfy the expression,

$$\bar{\Pi} = c_m/(\phi_{\text{SAP}} - \phi_m), \tag{8.34}$$

and the fitting shows that $\phi_{\text{SAP}} = 0.643$. Eq. (8.34) is appropriate here as it also

Table 8.1: The parameters for the model of glassy suspension rheology in Eq. (8.32)–(8.35) and Eq. (8.43).

K_μ	2.85	μ_G	0.03	$\bar{\Pi}_G$	3.5
α_μ	0.485	ϕ_G	0.585	c_m	0.202
K_ϕ	0.283	μ_{SAP}	0.308	β_y	0.211
α_ϕ	0.40	ϕ_{SAP}	0.643	K_d	0.037

describes the pressure of nearly jammed hard-sphere systems [111]. A check for the validity of ϕ_{SAP} is that, by shifting the experimental data upwards by $(\phi_{\mathrm{SAP}} - \phi_c)$ in Fig. 8.6b, the shifted results smoothly connect the non-Brownian ASD simulations near $I_v \approx 0.1$. Therefore, with non-Brownian experimental results and extrapolation, the $\bar{\Pi} \to \infty$ limit of the flow-arrest point, the SAP, is $(\mu_{\mathrm{SAP}}, \phi_{\mathrm{SAP}}) = (0.308, 0.643)$.

Finally, the following expression describes the relation between ϕ_m and μ_m in the inset of Fig. 8.10:

$$\frac{\mu_{\mathrm{SAP}} - \mu_m}{\mu_{\mathrm{SAP}} - \mu_G} = \left(\frac{\phi_{\mathrm{SAP}} - \phi_m}{\phi_{\mathrm{SAP}} - \phi_G}\right)^{\beta_y}, \tag{8.35}$$

with $\beta_y = 0.211$. Eq. (8.32)–(8.35) present a simple model for the rheology glassy suspensions valid for imposed pressure $\bar{\Pi} > \bar{\Pi}_G$. Table 8.1 summarizes the model parameters. In Fig. 8.6 the model results in the glassy limit at $\bar{\Pi} = \bar{\Pi}_G$ and the jamming limit at $\bar{\Pi} \to \infty$ are shown in dashed lines and the region bounded by these lines are colored yellow to show the glassy region. Fig. 8.6 shows that the simple model is valid near the flow arrest transitions for $I_v \lesssim 0.1$. At higher I_v, the model underestimates μ, and cannot capture the qualitative trend of the changes in ϕ when $\phi < 0.4$. Compared to models based on volume fractions [21, 112], the rheology model in Eq. (8.32)–(8.35) is simple yet powerful, with Eq. (8.32) and (8.33) highlighting the dominance of jamming physics, and Eq. (8.34) and (8.35) describing the adjustments from thermal fluctuations.

The flow map

Fig. 8.11 presents the μ-ϕ flow map at various imposed pressures $\bar{\Pi}$. The flow map is qualitatively similar to the results without HIs [25]. At a given $\bar{\Pi}$, the suspension dilates with increasing μ. The zero shear limit corresponds to $\mu \to 0$ in Fig. 8.11. For liquid-like suspensions, ϕ in the zero shear limit asymptotes the equilibrium value corresponds to the imposed pressure $\bar{\Pi}$. At $\bar{\Pi} \geq 3.5$, the glassy suspensions stops to flow when $\mu < \mu_m$ as the imposed stress is less than the yield stress σ_m. In Fig. 8.11, a region of arrested states emerges at the bottom right corner. The boundary for the arrested region, i.e., the yield surface, is shown in

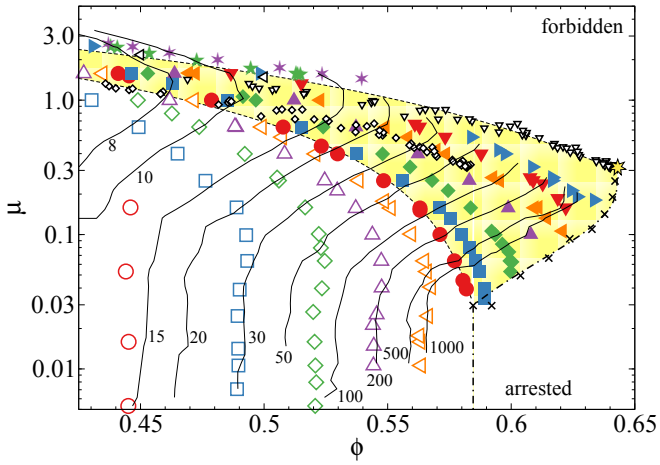

Figure 8.11: (Color online) The *macroscopic* friction coefficient $\mu = \sigma/\Pi$ as functions of the volume fraction ϕ over a wide range of imposed pressures $\bar{\Pi}$ for constant stress and pressure simulations. Also shown are the original and shifted non-Brownian experiments Boyer et al. [24], and the ASD simulations of Sierou and Brady [54]. The shifted experimental results shift the volume fraction data by $(\phi_{\text{SAP}} - \phi_c)$ with $\phi_c = 0.585$. The legends are identical to Fig. 8.6. The shaded region bounded by the dashed lines are from the rheology model outlining the region of glassy behavior. The viscosity contours up to $\eta_s/\eta_0 = 10^3$ are shown as solid lines with annotated viscosity. The crosses show the arrest location (μ_m, ϕ_m) at different imposed pressures, and the dash-dotted line outlines the yield surface from Eq. (8.35). The Shear Arrest Point (SAP) is highlighted as a star at the intersection of the arrested, the inaccessible, and the flowing region.

crosses in Fig. 8.11. With increasing imposed pressure $\bar{\Pi}$, the limiting friction coefficient μ_m increases until reaching the non-Brownian limit μ_{SAP}. That μ_m grows with increasing imposed pressure suggests that $\delta\sigma_m/\delta\Pi \geq \mu_m$, with the equal sign established at the SAP. That is, increasing the imposed pressure causes a larger increase in the yield stress $\delta\sigma_m$ predicted by the current limiting friction coefficient $\mu_m\delta\Pi$ until reaching the non-Brownian limit. In the $\bar{\Pi} \to \infty$ limit, the suspension dynamics are expected to collapse to the non-Brownian behaviors. With $\phi \leq 0.55$, the high-pressure data collapse is evident for $\bar{\Pi} = 100$ and $\bar{\Pi} = 200$. However, at larger ϕ, the constant stress and pressure simulation results only show a tendency to collapse. In Fig. 8.11, the non-Brownian limit is established by the ϕ-shifted experimental results. Since the hydrodynamic simulations can capture the suspension behaviors with HIs, unlike simulations without HIs [25], shifting the experimental friction coefficient is not necessary. This also confirms the mean-field hydrodynamic arguments in our earlier work. In the μ-ϕ flow map, the region beyond

the non-Brownian limit is physically inaccessible, and is shown as "forbidden" in Fig. 8.11. At the intersection of the forbidden, the arrested, and the flowing regions, the SAP emerges at the highest volume fraction attainable in the flowing suspensions.

In Fig. 8.11, the glassy suspension behaviors from the rheology model are shaded in yellow. The regions are bounded by three curves: two outline the $\mu(\phi)$ behaviors at $\bar{\Pi} = \bar{\Pi}_G$ and $\bar{\Pi} \to \infty$, one from the yield surface in Eq. (8.35). Note that at ϕ_G, the yield surface is vertical up to the glassy friction coefficient μ_G as we assume a physical scenario predicted by the mode-coupling theory [110, 113]: that as soon as the volume fraction exceeds ϕ_G, the suspension develops a finite static yield stress corresponding to μ_G. The glassy region predicted by the rheology model agrees well with the simulation and experimental results near the flow-arrest transitions.

Fig. 8.11 also shows the shear viscosity contours up to $\eta_s/\eta_0 = 10^3$. The contours show that, at a constant volume fraction $\phi \leq 0.57$, the shear viscosity first decreases and then increases with increasing μ, suggesting continuous shear thickening, which is also observed in constant volume simulations [8, 32, 33]. Continuous shear thickening arises from HIs among particles by forming "hydroclusters" in the suspensions. However, with $\phi > 0.57$, shear thickening behaviors disappear from the viscosity contours. One may argue that in the constant stress and pressure simulations, the strain rates at high volume fractions are not high enough to reveal the shear thickening behaviors. For example, at $\phi = 0.60$, the strain rate Péclet number corresponding to an impose pressure $\bar{\Pi} = 50$ is $\mathrm{Pe}_{\dot{\gamma}} \approx 6.1$, as in Fig. 8.1b and 8.1d, $\phi = 0.60$ corresponds to $\mathrm{Pe}_\sigma = 400$ and $\eta_s/\eta_0 = 65$, and $\mathrm{Pe}_{\dot{\gamma}}$ can be obtained from Eq. (8.24). However, for dense suspensions, experiments [114] and simulations [33] also show that the onset $\mathrm{Pe}_{\dot{\gamma}}$ of shear thickening behaviors decreases with increasing volume fractions, and $\mathrm{Pe}_{\dot{\gamma}} \approx 6$ may not be low at this volume fraction. Another possibility is that the continuous shear thickening disappears at high ϕ, as the decreasing Brownian viscosity contribution η^{B} from a high value masks the increase in the flow viscosity η^{E}, and that η^{E} cannot grow without bound as any small steric effects may significantly limit its value.

To understand the lack of shear thickening in Fig. 8.11 at high ϕ, we performed constant stress and *volume* simulations over a wide range of imposed stresses at $\phi = 0.6$. Fig. 8.12 presents the resulting shear viscosity η_s and its flow and Brownian contributions, η^{E} and η^{B}, as functions of Pe_σ ranging from 10 to 10^5. The strain rate Péclet number $\mathrm{Pe}_{\dot{\gamma}}$ corresponding to $\mathrm{Pe}_\sigma = 10^5$ is $\mathrm{Pe}_{\dot{\gamma}} = 1537$. With increasing Pe_σ, η^{B} decreases drastically towards zero. However, η^{E} increases

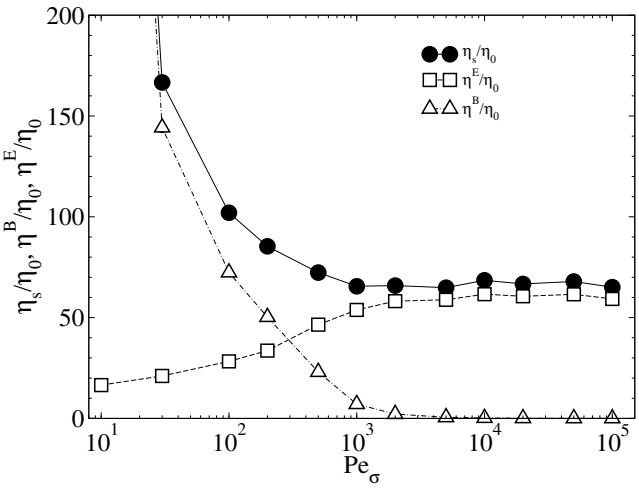

Figure 8.12: The shear viscosity η_s/η_0 and its flow and Brownian contributions, η^{E}/η_0 and η^{B}/η_0 as functions of stress Péclet number in constant stress and *volume* simulations at $\phi = 0.60$ with the particle size polydispersity p.d. = 0.1. The duration of each simulation is $\tau = 2000$ with a step size $\Delta\tau = 0.01$.

mildly, and reaches a high Pe_σ limiting value. Because the excluded volume radius is slightly larger than the hydrodynamic radius in the simulations, η^{E} cannot not continuously grow with Pe_σ. The effect of this interparticle force is evident from the difference between η^{E} and η_s in the $\mathrm{Pe}_\sigma \to \infty$ limit. The net result is that η_s exhibits only shear thinning with increasing Pe_σ until reaching the high Pe_σ viscosity. The increase in η^{E} is masked by the strong reduction of η^{B}. Therefore, in hydrodynamic simulations, even weak excluded volume effects can make the shear thickening disappear at high ϕ.

Fig. 8.11 and 8.12 also suggest that the experimentally observed discontinuous shear thickening [114, 115] cannot occur in hard-sphere suspensions with pure HIs. Other mechanisms must be operative. A popular interpretation of the discontinuous shear thickening is the frictional contact mechanism [53, 116, 117]. Although appealing for its simplicity and effectiveness, this interpretation directly uses the *macroscopic* concept of frictional interactions in granular materials to colloidal particles, which are several orders of magnitude smaller.

The viscosity contours in Fig. 8.11 near flow-arrest transitions are almost parallel to the arrest boundary shown in dash dotted line. From Eq. (8.32) and (8.33), the

suspension viscosity η_s can be expressed in $\delta\phi$ as,

$$\frac{\eta_s}{\eta_0} = \mu_m \left(\frac{\delta\phi}{K_\phi}\right)^{-\frac{1}{\alpha_\phi}} + K_\mu \left(\frac{\delta\phi}{K_\phi}\right)^{\frac{\alpha_\mu - 1}{\alpha_\phi}} . \tag{8.36}$$

Since both exponents α_μ and α_ϕ are positive, η_s exhibits a two-exponent divergence with respect to $\delta\phi$. At small $\delta\phi$, the divergence is characterized by the exponent $-1/\alpha_\phi$, and at large $\delta\phi$, the divergence is characterized by $(\alpha_\mu - 1)/\alpha_\phi$. Equating the first and the second terms in Eq. (8.36) leads to the crossover the volume fraction difference $\delta\phi_c$ and the crossover shear viscosity η_{sc} separating the two divergence regimes:

$$\delta\phi_c = K_\phi \left(\frac{\mu_m}{K_\mu}\right)^{\frac{\alpha_\phi}{\alpha_\mu}} \quad \text{and} \quad \frac{\eta_{sc}}{\eta_0} = 2\mu_m \left(\frac{\mu_m}{K_\mu}\right)^{-\frac{1}{\alpha_\mu}} . \tag{8.37}$$

With the parameters in Table 8.1, the crossover point in the glass limit is $(\delta\phi_c, \eta_{sc}/\eta_0) = (0.0066, 718)$ and in the jamming limit is $(0.045, 60.5)$. Since there is an observation window of $\delta\phi$ and η_s, the crossover is more apparent with large $\delta\phi_c$ and small η_{sc}. For example, the crossover point for non-Brownian soft-potential systems in the zero-pressure limit [62] is $(0.0183, 6.3)$, making the two-exponent behaviors apparent.

For non-Brownian suspensions, Boyer et al. [24] found $\alpha_\phi = 0.5$, leading to a leading order viscosity divergence $\eta_s \propto \delta\phi^{-2}$. In simulations without HIs, a similar viscosity divergence was discovered as in Eq. (8.1), with k_s and k_n independent of $\bar{\Pi}$, suggesting the dominance of the jamming physics. In fact, the universal viscosity divergence in Eq. (8.1) can also be interpreted using Eq. (8.32) and (8.33). Assuming that in Eq. (8.33), K_ϕ is now a function of the imposed pressure Π, and with a new set of limiting volume fractions ϕ_m, the volume fraction difference $\delta\phi = K_\phi(\Pi) I_v^{\alpha_\phi}$. Therefore, the universal shear viscosity η_s and the incremental normal viscosity η_n' divergences in Ref. [25] suggests that the constants k_s and k_n in Eq. (8.1) are

$$k_s = \mu_m K_\phi^{\frac{1}{\alpha_\phi}} \quad \text{and} \quad k_n = \left(1 - \frac{\Pi^{\text{eq}}}{\Pi}\right) K_\phi^{\frac{1}{\alpha_\phi}}, \tag{8.38}$$

also with $\alpha_\phi = 0.5$. Here, $\Pi^{\text{eq}}(\phi) \neq \Pi$ at the flow arrest transitions as the suspensions have to dilate before flowing. This interpretation relies on the existence of a yield stress and yield pressure, and does not reveal K_μ and α_μ in Eq. (8.33). Recently, the exponent $\alpha_\phi = 0.5$ is also discussed using the Herschel-Bulkley rheology of the osmotic pressure [118]. Despite the same underlying physical messages, the model in Sec. 8.4 is more general due to the additional description on the friction

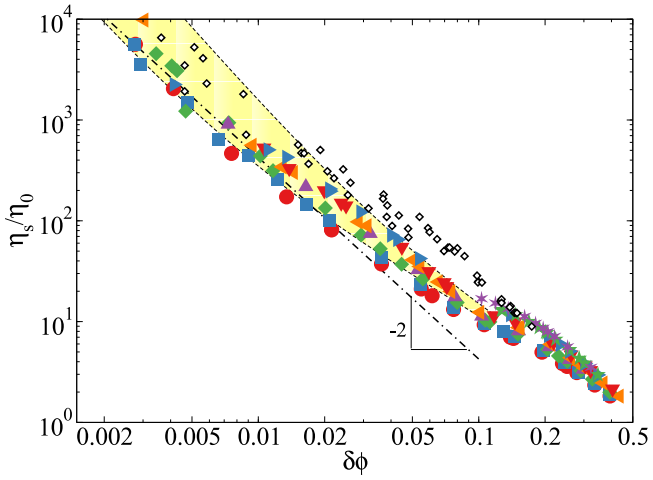

Figure 8.13: (Color online) The shear viscosity η_s/η_0 as a function of the volume fraction distance to the arrest $\delta\phi = (\phi_m - \phi)$ for glassy suspensions with $\bar{\Pi} \geq 3.5$. The non-Brownian experimental results of Boyer et al. [24] are also presented as black open diamonds. The yellow shaded region bounded by dashed lines are predictions from Eq. (8.36). The dash-dotted line shows an alternative viscosity divergence $\propto \delta\phi^{-2}$. The legends are identical to Fig. 8.6.

coefficient μ. More importantly, although the model associated with Eq. (8.1) works for simulations without HIs, it does not fit the SEASD results well.

Fig. 8.13 examines the viscosity divergence near the flow-arrest transition, and presents the shear viscosity η_s as functions of the the volume fraction difference from the arrest $\delta\phi = \phi_m - \phi$ for glassy suspensions with $\bar{\Pi} \geq 3.5$. The glass and the jamming limits of Eq. (8.36) are also presented in Fig. 8.13 in dashed lines. The constant stress and pressure simulation results agree with Eq. (8.36), and generally lie in an area bounded by the glass and the jamming limits highlighted in yellow. However, the non-Brownian experimental results [24] are rather scattered, as the small discrepancies in Fig. 8.10 are amplified in Fig. 8.13. Due to the disparate crossover points in the glass and in the jamming limits, near $\delta\phi = 0.01$ the viscosity appears to diverge at two different exponents. Moreover, by focusing on the data with $\eta_s/\eta_0 > 100$, the dash-dotted line Fig. 8.13 suggests that a divergence of $\delta\phi^{-2}$ also loosely describes the simulation results. That the data are close to the crossover viscosity η_{sc} leads to the ambiguity in the divergence exponent, i.e., any exponent between $-1/\alpha_\phi$ and $(\alpha_\mu - 1)/\alpha_\phi$ may appear reasonable.

Finally, the divergence of the the normal viscosity, $\eta_n = \Pi/\dot{\gamma}$ [24], is shown in Fig. 8.6a, as the inverse scaled normal viscosity is the viscous number $I_v = \eta_0/\eta_n$.

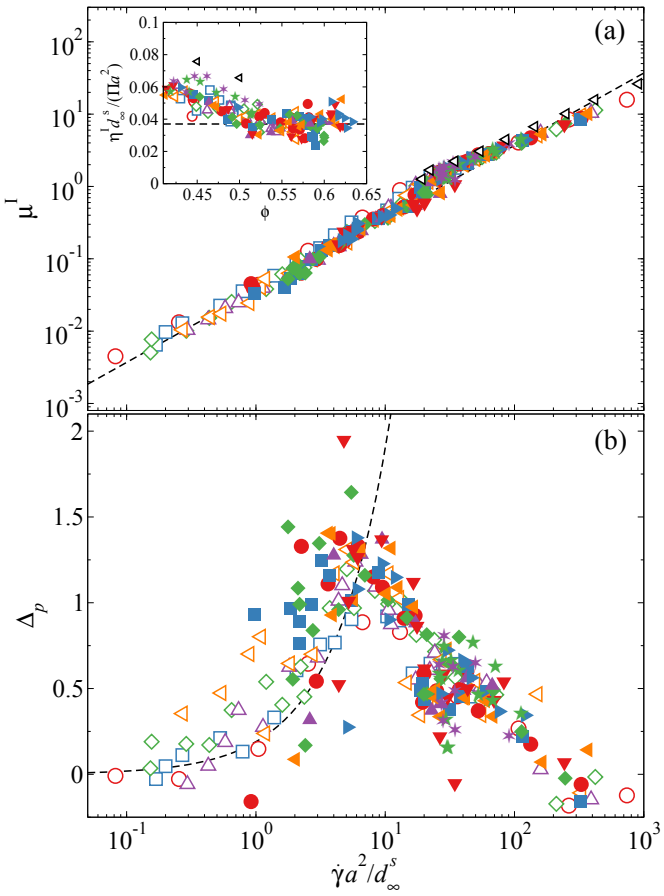

Figure 8.14: (Color online) (a) The interaction friction coefficient $\mu^{\rm I} = \mu - (1 + \frac{5}{2}\phi)I_v$ as functions of the strain rate scale $\dot{\gamma}a^2/d_\infty^s$. The dashed line indicates the linear relation $\mu^I = K_d\dot{\gamma}a^2/d_\infty^s$ with K_d in Table 8.1. The black open left triangles are the non-Brownian ASD simulation results [43, 54]. Inset: the product $(\eta^{\rm I}d_\infty^s/(\Pi a^2)$ as functions of volume fraction ϕ. The interaction viscosity $\eta^{\rm I} = \mu^{\rm I}/I_v$. (b) The peak difference $\Delta_p = \max(g_{\rm comp}) - \max(g_{\rm ext})$ as functions of the strain rate scale $\dot{\gamma}a^2/d_\infty^s$. The dashed lines represents a linear relation $\Delta_p = K_p\dot{\gamma}a^2/d_\infty^s$ with $K_p = 0.19$. In (a) and (b), the legends are identical to those of Fig. 8.6.

Therefore, from Eq. (8.33) we have $\eta_n/\eta_0 = (\delta\phi/K_\phi)^{-1/\alpha_\phi}$ with the constants from Table 8.1.

8.5 Universal behaviors for dense suspensions

Here we explore the universal connection among suspension structure, diffusion, and rheology for *all* imposed pressures. These relations are valid regardless of the way the external forces are imposed, and reveal the fundamental suspension behaviors.

An effective Stokes-Einstein-Sutherland relation

The pressure scaled diffusivity d^s_∞/d_Π in Fig. 8.6a and the suspension shear viscosity η_s/η_0 in Fig. 8.9 are close to up-down mirror images of each other with respect to the viscous number I_v, i.e., where η_s/η_0 is high, the corresponding d^s_∞/d_Π is low, suggesting that the product $\eta_s d^s_\infty/(\eta_0 d_\Pi)$ may be constant. The exception is the $I_v \gg 1$ limit, where the shear viscosity η_s/η_0 collapses stronger than d^s_∞/d_Π, as in the dilute limit $\eta_s \to \eta_0$, but d^s_∞ does not approach d_Π. To eliminate this exception, we introduce an interaction stresses σ^{I} that removes the single-particle contributions, i.e., $\sigma^{\mathrm{I}} = \sigma - (1 + \frac{5}{2}\phi)\eta_0\dot{\gamma}$. This stress definition leads to the interaction friction coefficient μ^{I} and the interaction viscosity η^{I},

$$\mu^{\mathrm{I}} = \mu - (1 + \tfrac{5}{2}\phi)I_v \quad \text{and} \quad \eta^{\mathrm{I}}/\eta_0 = \mu^{\mathrm{I}}/I_v. \tag{8.39}$$

In the $I_v \ll 1$ limit, $\mu^{\mathrm{I}} \to \mu$ and $\eta^{\mathrm{I}} \to \eta_s$. The inset of Fig. 8.14a shows the product $\eta^{\mathrm{I}} d^s_\infty/(\eta_0 d_\Pi) = \eta^{\mathrm{I}} d^s_\infty/(\Pi a^2)$ as functions of the volume fraction ϕ for *all* imposed pressures $\bar{\Pi}$.

The combination $\eta^{\mathrm{I}} d^s_\infty/(\Pi a^2)$ collapses impressively without any fitting parameters over a wide parameter space with over 5 orders of magnitude in Pe_σ and over 2 orders of magnitude in $\bar{\Pi}$. The collapsed results decrease slightly from 0.06 to 0.038 with increasing ϕ up to $\phi \approx 0.52$, and become approximately constant afterwards. Consistent with the observation of the up-down mirror images in Fig. 8.6a and Fig. 8.9, the inset of Fig. 8.14a suggests an effective SES relation for $\phi \gtrsim 0.52$, i.e.,

$$d^s_\infty = \frac{k_{\mathrm{B}} T_{\mathrm{eff}}}{6\pi\eta^{\mathrm{I}} a_z}, \tag{8.40}$$

with the effective temperature

$$k_{\mathrm{B}} T_{\mathrm{eff}} = \Pi a_z^3 \tag{8.41}$$

and the characteristic length scale $a_z \approx 0.8a$. Eq. (8.40) explicitly confirms the idea of effective temperature discussed in Sec. 8.4. It is valid for non-equilibrium sheared suspensions with both strong and weak thermal fluctuations, and, as is shown in the companion paper [26], is not affected by HIs. The characteristic scale a_z is close to the size of the activation zone in the shear transformation zone interpretation of hard-sphere rheology [119]. In the high shear limit, the effective temperature is proportional to the strain rate, $T_{\mathrm{eff}} \propto \dot{\gamma}$, consistent with other definitions of effective temperatures [13, 96]. In particular, the effective temperature defined in the experiments of Eisenmann et al. [96] is proportional to the shear stress,

since they focused on only one volume fraction at low strain rate. As is shown in Fig. 8.6c, with $I_v \to 0$, $\sigma = \mu_m \Pi$, i.e., both σ and Π are suitable for defining an effective temperature near the flow-arrest transitions. However, for a universal collapse shown in the inset of Fig. 8.14a, $T_{\text{eff}} \propto \Pi$ is necessary. In the limit of dilute equilibrium suspensions, the effective temperature is restored to the actual temperature $T_{\text{eff}} \to T$ and $a_z \to a$. Unlike other studies [90, 92, 95], here the base state is the infinitely dilute equilibrium suspension. Both the imposed flow and the presence of particles drive the system from the base state. The effective SES relation in Eq. (8.40) suggests a novel mean-field perspective on the rheology of non-equilibrium colloidal suspensions, highlighting the importance of osmotic pressure.

The main figure of Fig. 8.14a shows another perspective of the effective SES relation, and presents the interaction friction coefficient μ^{I} as a function of the long-time Péclet number,

$$\overline{\text{Pe}} = \dot{\gamma} a^2 / d^s_\infty = I_v d_\Pi / d^s_\infty, \tag{8.42}$$

i.e., the strain rate scaled by the vorticity direction long-time self-diffusivity. In the high shear limit, the long-time diffusivity with fixed ϕ becomes proportional to the strain rate, $d^s_\infty \propto \dot{\gamma}$ [33, 96], and $\overline{\text{Pe}}$ becomes a constant. In contrast, a larger $\overline{\text{Pe}}$ range can be accessed using constant stress and pressure rheology due to suspension dilation.

Without any fitting parameters, *all* simulation data collapse onto a universal curve in Fig. 8.14a. The collapsed μ^{I} is linear to the scaled strain rate up to $\overline{\text{Pe}} \approx 10$, becomes slightly scattered at $\overline{\text{Pe}} \approx 20$, and collapses again. The collapsed data are adequately described by the following linear relation,

$$\mu^{\text{I}} = K_d \overline{\text{Pe}}, \tag{8.43}$$

where the constant $K_d = 0.037$. Scaling the strain rate with the diffusivity in the velocity gradient direction gives similar results. The diffusivity prediction from Eq. (8.43) in the glass and the jamming limit are presented in Fig. 8.9.

For liquid-like suspensions, the particles can diffuse even without flow, and therefore $\overline{\text{Pe}}$ can reach low values. In Fig. 8.14a, the minimum is reached at $\bar{\Pi} = 1$ with $\overline{\text{Pe}} \approx 0.08$. However, for glassy suspensions, Fig. 8.14a shows that only $\overline{\text{Pe}} \gtrsim 1$ is possible. Therefore, the rate of dispersion, d^s_∞ / a^2, is at most as fast as the rate of convection, characterized by $\dot{\gamma}$, i.e., the particle diffusion is driven by the flow, not by the thermal fluctuations. This is because for glassy suspensions, the at-rest

diffusivity $d_T/d_0 \ll 1$ leading to an effective Péclet number $\mathrm{Pe}_T \gg 1$ for any finite $\dot{\gamma}$, and therefore the physics of non-Brownian jamming dominates the suspension dynamics [25]. Moreover, the collapsed results also suggest that the volume fraction ϕ is unimportant.

The lowest imposed pressure corresponds to $\overline{\mathrm{Pe}} \approx 1$ in glassy suspensions is $\bar{\Pi} = 3.5$, and the corresponding friction coefficient $\mu^{\mathrm{I}} \approx 0.03$ in Fig. 8.14a. Therefore, Fig. 8.14a suggests that as soon as the suspension becomes glassy, a finite yield stress emerges discontinuously, consistent with the mode-coupling theory predictions [113] and the rheology model presented in Sec. 8.4. At this limit, since the suspension only begins to flow, $I_v \ll 1$ and therefore $\mu^{\mathrm{I}} \to \mu$. Therefore, Fig. 8.14a independently validates the glass transition friction coefficient, $\mu_G = 0.03$, in the rheology model of Sec. 8.4.

Fig. 8.14a also predicts the suspension diffusion near the athermal jamming limit. The non-Brownian ASD simulation results up to $\phi = 0.50$ [43, 54] are presented in black open left triangles and agree well with simulations at finite $\bar{\Pi}$ along the same master curve of Eq. (8.43). The long-time Péclet number $\overline{\mathrm{Pe}}$ increases with decreasing ϕ. Therefore, the diffusivity at the SAP can be read from the figure. With the experimental SAP friction coefficient $\mu_{\mathrm{SAP}} = 0.308$, the corresponding $\overline{\mathrm{Pe}} \approx 8.3$ in Fig. 8.14a, suggesting a long-time self-diffusivity $d^s_\infty = 0.12\dot{\gamma}a^2$. Surprisingly, the maximum diffusivity in non-Brownian suspensions is found at the highest volume fraction near the SAP due to strong interactions with neighboring particles.

Structure, rheology, and dynamics

Fig. 8.14b explores the connection between the suspension structures and dynamics by plotting the compressional and extensional axes pair distribution function peak difference,

$$\Delta_p = \max(g_{\mathrm{comp}}) - \max(g_{\mathrm{ext}}), \tag{8.44}$$

as functions of $\overline{\mathrm{Pe}}$. The peak difference Δ_p approximates the structural integral $\int \hat{r}\hat{r}g(2,\Omega)\mathrm{d}\Omega$. Despite some data scattering, a trend in how Δ_p changes with $\overline{\mathrm{Pe}}$ is evident: with increasing $\overline{\mathrm{Pe}}$, Δ_p first increases, reaches a maximum at $\overline{\mathrm{Pe}} \approx 7$, and then decreases. With fixed ϕ, the peak difference Δ_p grows with the suspension structural anisotropy, and constant Π and σ, the influences of suspension dilation is also important.

When $\overline{\mathrm{Pe}} \lesssim 7$, the growth of Δ_p with $\overline{\mathrm{Pe}}$ is roughly linear, shown in a dashed line in

Fig. 8.14b,

$$\Delta_p = K_p \overline{\mathrm{Pe}}, \tag{8.45}$$

with the constant $K_p = 0.19$. Combining with Fig. 8.14a, the results suggests that the suspension interaction shear stress $\sigma^{\mathrm{I}} \propto \Delta_p \Pi$, i.e., the suspension shear stress contains multiplicative contributions from the osmotic pressure and the structural anisotropy. Moreover, for liquid-like suspensions, the structural anisotropy increases from 0 at low $\overline{\mathrm{Pe}}$. However, for glassy suspensions, at the onset of flow $\overline{\mathrm{Pe}} \approx 1$, the structural anisotropy is already finite, confirming that the structural change precedes flow as is shown in Fig. 8.1d.

At a critical $\overline{\mathrm{Pe}}$, the anisotropy reaches a maximum before the suspension begins to dilate, leading to Δ_p reduction. Here, the critical $\overline{\mathrm{Pe}}$ is roughly the same for all $\bar{\Pi}$, as particle diffusion is intimately connected to the suspension structures. Since $\overline{\mathrm{Pe}}$ is the inverse of the diffusivity, Fig. 8.14b suggests that the structural change is due to the limited diffusion comparing to the flow. Further reduction in Δ_p appears branched near $\overline{\mathrm{Pe}} \approx 20$, where μ^I also becomes more scattered in Fig. 8.14a. Here, the two branches exhibit different Δ_p reduction with respect to $\overline{\mathrm{Pe}}$. Since results with apparent string formation are not considered in Fig. 8.14b, the more sensitive branch may arise from the formation of subtle structures not as obvious as the strings. The less sensitive branch, on the other hand, arises from suspension dilation in the high shear limit. From Fig. 8.2 and 8.3, this reduction is also related to the vorticity direction particle alignment.

8.6 Summary and Conclusions

We studied the rheology, structure, and dynamics of the constant stress and pressure rheology of dense colloidal suspensions over a wide parameter space including 5 decades of imposed stresses and 2 decades of imposed pressures with HIs. To achieve this, we developed a computational method based on the SEASD method to impose the constant stress and pressure constraint by solving the instantaneous suspension mechanical balance. To further improve the computational speed, we adopted the near-field Brownian approximation, which used a mean-field approximation for the far-field part of the Brownian forces.

With fixed pressure, the suspension dilates and continues to shear thin with increasing imposed stresses. The suspension behaviors can be broadly divided to the liquid-like and glassy. Liquid-like suspensions do not exhibit flow-arrest transitions at low imposed stresses, but glassy suspensions do. Structurally, liquid-like

suspensions are homogeneous at all imposed stresses, and high pressure glassy suspensions show string order formation with increasing imposed stresses. Further stress increase melts the string structures. At high imposed stress, the particles exhibit preferential alignment in the vorticity direction due to the closed trajectory of particle pairs in simple shear flows. The particle long-time self-diffusivity of colloidal exhibits little anisotropy at low imposed stress. The diffusivity decreases drastically with string order formation. At high imposed stresses after string melting, the diffusivity show increasing anisotropy in the vorticity and the velocity gradient directions.

We examined the flow behaviors of amorphous suspensions using a granular perspective, and characterized the rheology using the macroscopic friction coefficient μ and the viscous number I_v. Our simulation results agree well with the non-Brownian experiments [24] and ASD simulations [43, 54] including the shear viscosity η_s, the normal stress differences N_1 and N_2, and the long-time self-diffusivity d^s_∞. By constructing a μ-ϕ flow map, we also found that shear thickening occurs when the volume fractions are held constant with $\phi < 0.57$.

We discovered universal connections among the suspension rheology, diffusion, and diffusion in parameter-free data collapses. By introducing an interaction friction coefficient μ^I, we discovered that $\mu^I \propto \dot{\gamma}a^2/d^s_\infty$, suggesting that the suspension dynamics are controlled by an effective temperature proportional to the osmotic pressure, $T_{\text{eff}} \propto \Pi$, and the diffusivity can be predicted via an effective SES relation. Moreover, the structural features of the suspension, characterized by the peak difference Δ_p, also collapse for different imposed pressures. Our discoveries here suggests that the suspension dynamics can be described in a mean-field fashion using the concept of effective temperature T_{eff}. Our novelty in this work is that the effective temperature is connected to pressure, and is based on a base state with both $\dot{\gamma} \to 0$ and $\phi \to 0$.

Based on the simulation results, we developed a model for glassy suspensions near the flow-arrest transitions. We found that the friction coefficient and the volume fraction changes from the arrest value following universal power laws of I_v regardless of the imposed pressures $\bar{\Pi}$, suggesting that physics of jamming dominates the glassy suspension behaviors, and that the thermal fluctuations only affect the arrest locations. Our model is the only available model that can simultaneously predict the rheological and the diffusive behaviors of glassy suspensions. With a complementary model for liquid-like suspensions, we can completely describe the

suspension behaviors. However, the development of a rheology model for liquid-like suspension is deferred to future works.

This study is the first comprehensive hydrodynamic investigations on the behaviors of dense suspensions, and demonstrate that the influences of HIs are quantitative for amorphous systems. Our work suggests that the flowing behaviors of dense suspensions should be described in a mean-field fashion using the concept of effective temperatures. Our work also points out that pressure is an extremely crucial quantity in understanding the behaviors of non-equilibrium flowing systems.

8.A Computing hydrodynamic interactions

We compute HIs in polydisperse hard-sphere Brownian suspensions using the SEASD method with near-field Brownian approximation [56]. The framework of Stokesian Dynamics [57] resolves the long-range non-pairwise-additive far-field and diverging near-field lubrication interactions in suspension hydrodynamics by combining the mobility and the resistance formalism. It computes the grand resistance tensor $\boldsymbol{\mathcal{R}}$ as

$$\boldsymbol{\mathcal{R}} = (\boldsymbol{\mathcal{M}}^{\infty})^{-1} + (\boldsymbol{\mathcal{R}}_{2\mathrm{B}} - \boldsymbol{\mathcal{R}}^{\infty}_{2\mathrm{B}}), \tag{8.46}$$

with $\boldsymbol{\mathcal{M}}^{\infty}$ the far-field grand mobility tensor and $(\boldsymbol{\mathcal{R}}_{2\mathrm{B}} - \boldsymbol{\mathcal{R}}^{\infty}_{2\mathrm{B}})$ the pairwise grand resistance tensor from the exact solutions of two-body hydrodynamic problems with the far-field contribution removed. The far-field resistance contribution $\boldsymbol{\mathcal{R}}^{\infty}_{2\mathrm{B}}$ is the inversion of $\boldsymbol{\mathcal{M}}^{\infty}$ for two particles. Inverting $\boldsymbol{\mathcal{M}}^{\infty}$ captures the long-range non-pairwise-additive aspect of the HIs, and $(\boldsymbol{\mathcal{R}}_{2\mathrm{B}} - \boldsymbol{\mathcal{R}}^{\infty}_{2\mathrm{B}})$ recovers the near-field diverging lubrication interactions. In the SEASD method, the action of $\boldsymbol{\mathcal{M}}^{\infty}$ on a vector is computed using Spectral Ewald method [58, 59], and $(\boldsymbol{\mathcal{R}}_{2\mathrm{B}} - \boldsymbol{\mathcal{R}}^{\infty}_{2\mathrm{B}})$ is constructed pairwise with cutoff distance, currently set at $2(a_i + a_j)$ for each pair due to the short-range lubrication interactions.

The near-field Brownian approximation adopts a mean-field approach to treat the far-field HIs for $\boldsymbol{\mathcal{U}}^{\mathrm{B}}$ [Eq. (8.13)], $\Delta\boldsymbol{\mathcal{X}}^{\mathrm{B}}$ [Eq. (8.10)], and $\boldsymbol{S}^{\mathrm{B}}$ [Eq. (8.17)], and retains the full hydrodynamic computations for other quantities. In computing the Brownian-related quantities, the far-field grand mobility tensor $\boldsymbol{\mathcal{M}}^{\infty}$ is approximated as a diagonal matrix, using $d_s^{\mathrm{t,ff}}$ for the elements corresponding to the velocity-force coupling, and $d_s^{\mathrm{r,ff}}$ for the elements corresponding to the angular velocity-torque coupling. For the strain rate-stresslet coupling, the single-particle relation $\boldsymbol{E}^{\infty} = \boldsymbol{S}^{\mathrm{H}}/(\frac{20}{3}\pi\eta_0 a^3)$ is used. Here, $d_s^{\mathrm{t,ff}}$ and $d_s^{\mathrm{r,ff}}$ are the far-field short-time translational and rotational diffusion coefficients of equilibrium suspensions at the same composition and vol-

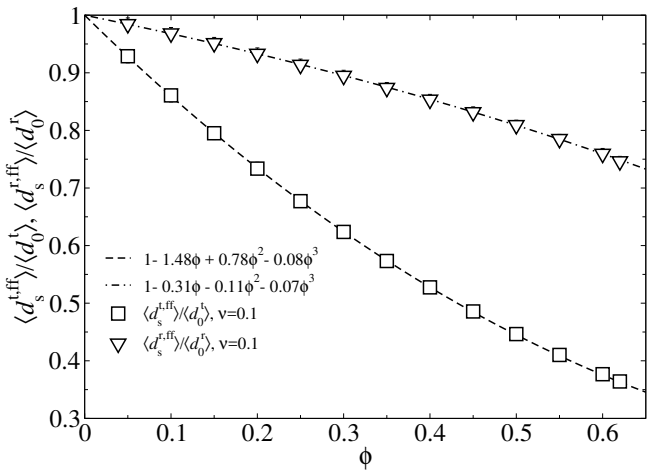

Figure 8.15: The mean far-field translational and rotational diffusion coefficients, $\left\langle d_s^{\mathrm{t,ff}}\right\rangle$ and $\left\langle d_s^{\mathrm{r,ff}}\right\rangle$, respectively, as functions of volume fraction ϕ for a polydisperse suspension with polydispersity p.d. = 0.1. The dashed and dash-dotted lines are cubic polynomial fit to the calculation results.

ume fractions. They can be obtained from static calculations without the near-field lubrication contributions.

In this work, we consider the polydisperse suspension an effective medium characterized by the mean single-particle translational and rotational diffusion coefficients $\left\langle d_0^{\mathrm{t}}\right\rangle = N^{-1}\sum_i d_{0,i}^{\mathrm{t}}$ and $\left\langle d_0^{\mathrm{r}}\right\rangle = N^{-1}\sum_i d_{0,i}^{\mathrm{r}}$, respectively, with $d_{0,i}^{\mathrm{t}} = k_{\mathrm{B}}T/(6\pi\eta_0 a_i)$ and $d_{0,i}^{\mathrm{r}} = k_{\mathrm{B}}T/(8\pi\eta_0 a_i^3)$, and compute a single effective far-field diffusion coefficient for all particle species. This approach eliminates the need to identify different particle species in the approximated far-field mobility tensor, and is consistent with the mean-field idea behind the near-field Brownian approximation.

Fig. 8.15 shows the mean far-field translational and rotational diffusion coefficients, $\left\langle d_s^{\mathrm{t,ff}}\right\rangle$ and $\left\langle d_s^{\mathrm{r,ff}}\right\rangle$, respectively, for polydisperse suspensions with polydispersity p.d. = 0.1 as functions of volume fraction ϕ. The configurations are generated by a polydisperse Lubachevsky-Stillinger algorithm [101, 102] followed by a brief equilibration [30]. The system size $N = 800$ and the species number $M = 10$, and each point in Fig. 8.15 is averaged over 500 independent configurations. Note that $\left\langle d_s^{\mathrm{t,ff}}\right\rangle$ exhibits a strong system size dependence proportional to $N^{\frac{1}{3}}$, and this effect has been corrected in Fig. 8.15 with the far-field high-frequency dynamic viscosity [56]. The finite size effect in $\left\langle d_s^{\mathrm{r,ff}}\right\rangle$ is negligible. The simulation results can be satisfactorily fit by a cubic polynomial in ϕ up to the close packing density. These fitted polynomials are used in the dynamic simulations for computing Brownian

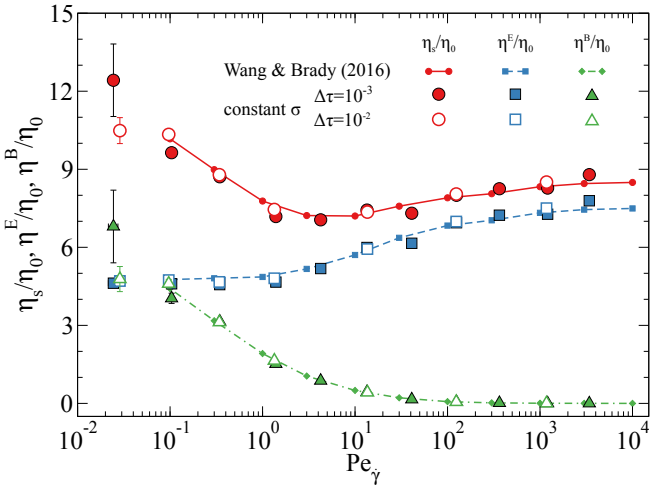

Figure 8.16: (Color online) The total suspension viscosity η_s/η_0 and its flow and Brownian contributions, η^{E}/η_0 and η^{B}/η_0, respectively, as functions of the strain rate Péclet number $\mathrm{Pe}_{\dot\gamma}$ for a bidisperse suspension with size ratio 2 and equal volume ratio at $\phi = 0.45$. All computations are from SEASD method with full hydrodynamic interactions. The lines are from constant strain rate simulations [56]. The symbols are from constant stress simulations with dimensionless step size $\Delta\tau = 10^{-3}$ (filled symbols) and $\Delta\tau = 10^{-2}$ (open symbols).

related quantities.

8.B Validation via constant stress simulations

As indicated in Sec. 8.2, with $\dot e = 0$, the constant stress and pressure algorithm reduces to the constant stress, fixed volume algorithm of Swan and Brady [66]. For homogeneous suspensions below the glass transition, imposing a constant stress is equivalent to imposing a corresponding strain rate at steady state. Therefore, the constant stress and pressure algorithm can be partially validated by comparing results from constant stress simulations with known constant strain rate data.

We performed constant stress simulations at different dimensionless time steps $\Delta\tau$ for bidisperse colloidal suspensions of size ratio 2 and equal volumes for both species at a total volume fraction $\phi = 0.45$ with full HIs. Fig. 8.16 compares the constant stress suspension shear viscosity, η_s, and its flow and Brownian contributions, η^{E} and η^{B}, respectively, with the constant strain rate results [56]. The constant stress results, originally expressed as functions of Pe_σ, are converted to functions of $\mathrm{Pe}_{\dot\gamma}$ using Eq. (8.24). Note that, for hard-sphere suspensions, the interparticle force does not contribute to the stress, and therefore $\eta^{\mathrm{P}} = 0$. Qualitatively, increasing $\mathrm{Pe}_{\dot\gamma}$ leads to rapid reduction in η^{B} and slow growth in η^{E}. At high Pe_σ, the Brownian viscosity

η^B reduces to zero but the flow viscosity η^E asymptotes a constant. As a result, the suspension viscosity η_s first decreases and then increases mildly with growing $\mathrm{Pe}_{\dot{\gamma}}$. A key feature of the constant volume rheology is the existence of a high-shear viscosity as $\mathrm{Pe}_{\dot{\gamma}} \to \infty$.

In Fig. 8.16, the good agreement between the constant stress results, shown in symbols, and the constant strain rate data, shown in dots, at least partially validate the constant stress and pressure algorithm in Sec. 8.2. In addition, Fig. 8.16 also compares the effect of the dimensionless time step size with $\Delta\tau = 10^{-2}$ and 10^{-3}. In the low $\mathrm{Pe}_{\dot{\gamma}}$ limit, the Brownian viscosity η^B at $\Delta\tau = 10^{-3}$ show larger fluctuations, but the flow contribution η^E with different time steps agree well. In the high $\mathrm{Pe}_{\dot{\gamma}}$ limit, on the other hand, η^B agrees well, but η^E exhibit small differences at different $\Delta\tau$, suggesting subtle differences in particle configurations. Despite these small quantitative differences, different time steps lead to the same suspension rheology, justifying using $\Delta\tau = 10^{-2}$ in most dynamic simulations in this work.

References

[1] W. B. Russel, D. A. Saville, and W. R. Schowalter, *Colloidal dispersions* (Cambridge University Press, 1991).

[2] R. J. Hunter, *Foundations of colloid science* (Oxford University Press, 2001).

[3] J. Mewis and N. J. Wagner, *Colloidal suspension rheology* (Cambridge University Press, 2013).

[4] M. Ballauff, J. M. Brader, S. U. Egelhaaf, M. Fuchs, J. Horbach, N. Koumakis, M. Krüger, M. Laurati, K. J. Mutch, G. Petekidis, M. Siebenbürger, T. Voigtmann, and J. Zausch, "Residual stresses in glasses", Phys. Rev. Lett. **110**, 215701 (2013).

[5] N. Koumakis, M. Laurati, S. U. Egelhaaf, J. F. Brady, and G. Petekidis, "Yielding of hard-sphere glasses during start-up shear", Phys. Rev. Lett. **108**, 098303 (2012).

[6] T. Sentjabrskaja, E. Babaliari, J. Hendricks, M. Laurati, G. Petekidis, and S. U. Egelhaaf, "Yielding of binary colloidal glasses", Soft Matter **9**, 4524 (2013).

[7] X. Cheng, J. H. McCoy, J. N. Israelachvili, and I. Cohen, "Imaging the microscopic structure of shear thinning and thickening colloidal suspensions", Science **333**, 1276 (2011).

[8] G. Bossis and J. F. Brady, "The rheology of brownian suspensions", J. Chem. Phys. **91**, 1866 (1989).

[9] H. M. Laun, "Rheological properties of aqueous polymer dispersions", Angewandte Makromolekulare Chemie **123/124**, 335 (1984).

[10] N. J. Wagner and J. F. Brady, "Shear thickening in colloidal dispersions", Phys. Today **62**, 27 (2009).

[11] C. D. Cwalina and N. J. Wagner, "Material properties of the shear-thickened state in concentrated near hard-sphere colloidal dispersions", J. Rheol. **58**, 949 (2014).

[12] L. Isa, R. Besseling, A. N. Morozov, and W. C. K. Poon, "Velocity oscillations in microfluidic flows of concentrated colloidal suspensions", Phys. Rev. Lett. **102**, 058302 (2009).

[13] R. G. M. van der Sman and H. M. Vollebregt, "Effective temperature for sheared suspensions: a route towards closures for migration in bidisperse suspension", Adv. Colloid Interface Sci. **185–186**, 1 (2012).

[14] M. Hermes, B. M. Guy, G. Poy, M. E. Cates, M. Wyart, and W. C. K. Poon, "Unsteady flow and particle migration in dense, non-brownian suspensions", J. Rheol. **60**, 905 (2016).

[15] A. J. Liu and S. R. Nagel, "Nonlinear dynamics: jamming is not just cool any more", Nature **396**, 21 (1998).

[16] A. J. Liu and S. R. Nagel, "The jamming transition and the marginally jammed solid", Annu. Rev. Condens. Matter Phys. **1**, 347 (2010).

[17] T. K. Haxton, M. Schmiedeberg, and A. J. Liu, "Universal jamming phase diagram in the hard-sphere limit", Phys. Rev. E **83**, 031503 (2011).

[18] W. B. Russel, N. J. Wagner, and J. Mewis, "Divergence in the low shear viscosity for brownian hard sphere dispersions: at random close packing or the glass transition?", J. Rheol. **57**, 1555 (2013).

[19] P. N. Pusey and W. van Megen, "Phase behaviour of concentrated suspensions of nearly hard colloidal spheres", Nature **320**, 340 (1986).

[20] P. Olsson and S. Teitel, "Athermal jamming versus thermalized glassiness in sheared frictionless particles", Phys. Rev. E **88**, 010301(R) (2013).

[21] A. Ikeda, L. Berthier, and P. Sollich, "Unified study of glass and jamming rheology in soft particle systems", Phys. Rev. Lett. **109**, 018301 (2012).

[22] G. Brambilla, D. El Masri, M. Pierno, L. Berthier, L. Cipelletti, G. Petekidis, and A. Schofield, "Probing the equilibrium dynamics of colloidal hard spheres above the mode-coupling glass transition", Phys. Rev. Lett. **102**, 085703 (2009).

[23] W. van Megen, T. C. Mortensen, S. R. Williams, and J. Müller, "Measurement of the self-intermediate scattering function of suspensions of hard spherical particles near the glass transition", Physical Review E **58**, 6073 (1998).

[24] F. Boyer, E. Guazzelli, and O. Pouliquen, "Unifying suspension and granular rheology", Phys. Rev. Lett. **107**, 188301 (2011).

[25] M. Wang and J. F. Brady, "Constant stress and pressure rheology of colloidal suspensions", Phys. Rev. Lett. **115**, 158301 (2015).

[26] M. Wang and J. F. Brady, "Constant stress and pressure rheology of colloidal suspensions: steady state behavior and dynamics near the flow-arrest transitions", In Preparation (2016).

[27] G. K. Batchelor, "Brownian diffusion of particles with hydrodynamic interaction", J. Fluid Mech. **74**, 1 (1976).

[28] G. K. Batchelor, "Sedimentation in a dilute dispersion of spheres", J. Fluid Mech. **52**, 245 (1972).

[29] R. J. Phillips, J. F. Brady, and G. Bossis, "Hydrodynamic transport properties of hard-sphere dispersions. i. suspensions of freely mobile particles", Phys. Fluids **31**, 3462 (1988).

[30] M. Wang and J. F. Brady, "Short-time transport properties of bidisperse suspensions and porous media: a stokesian dynamics study", J. Chem. Phys. **142**, 094901 (2015).

[31] J. F. Brady and G. Bossis, "Stokesian dynamics", Annu. Rev. Fluid Mech. **20**, 111 (1988).

[32] T. N. Phung, J. F. Brady, and G. Bossis, "Stokesian dynamics simulation of brownian suspensions", J. Fluid Mech. **313**, 181 (1996).

[33] D. R. Foss and J. F. Brady, "Structure, diffusion and rheology of brownian suspensions by stokesian dynamics simulation", J. Fluid Mech. **407**, 167 (2000).

[34] D. R. Foss and J. F. Brady, "Brownian Dynamics simulation of hard-sphere colloidal dispersions", J. Rheol. **44**, 629 (2000).

[35] S. R. Rastogi, N. J. Wagner, and S. R. Lustig, "Rheology, self-diffusion, and microstructure of charged colloids under simple shear by massively parallel nonequilibrium brownian dynamics", J. Chem. Phys. **104**, 9234 (1996).

[36] B. J. Ackerson and P. N. Pusey, "Shear-induced order in suspensions of hard spheres", Phys. Rev. Lett. **61**, 1033 (1988).

[37] B. J. Ackerson, "Shear induced order and shear processing of model hard sphere suspensions", J. Rheol. **34**, 553 (1990).

[38] X. Cheng, X. Xu, S. A. Rice, A. R. Dinner, and I. Cohen, "Assembly of vorticity-aligned hard-sphere colloidal strings in a simple shear flow", Proc. Natl. Acad. Sci. U. S. A. **109**, 63 (2012).

[39] A. K. Gurnon and N. J. Wagner, "Microstructure and rheology relationships for shear thickening colloidal dispersions", J. Fluid Mech. **769**, 242 (2015).

[40] F. Westermeier, D. Pennicard, H. Hirsemann, U. H. Wagner, C. Rau, H. Graafsma, P. Schall, M. P. Lettinga, and B. Struth, "Connecting structure, dynamics and viscosity in sheared soft colloidal liquids: a medley of anisotropic fluctuations", Soft Matter **12**, 171 (2016).

[41] X. Xu, S. A. Rice, and A. R. Dinner, "Influence of interlayer exchanges on vorticity-aligned colloidal string assembly in a simple shear flow", J. Phys. Chem. Lett. **4**, 3310 (2013).

[42] D. Leighton and A. Acrivos, "The shear-induced migration of particles in concentrated suspensions", J. Fluid Mech. **181**, 415 (1987).

[43] A. Sierou and J. F. Brady, "Shear-induced self-diffusion in non-colloidal suspensions", J. Fluid Mech. **506**, 285 (2004).

[44] A. M. Leshansky and J. F. Brady, "Dynamic structure factor study of diffusion in strongly sheared suspensions", J. Fluid Mech. **527**, 141 (2005).

[45] S. Kim and S. J. Karrila, *Microhydrodynamics* (Dover, 2005).

[46] D. L. Ermak and J. A. McCammon, "Brownian dynamics with hydrodynamic interactions", J. Chem. Phys. **69**, 1352 (1978).

[47] A. Mulero, ed., *Theory and simulation of hard-sphere fluids and related systems* (Springer, 2008).

[48] W. C. K. Poon, E. R. Weeks, and C. P. Royall, "On measuring colloidal volume fractions", Soft Matter **8**, 21 (2012).

[49] N. Koumakis, "A study on the effects of interparticle interactions on the dynamics, rheology and aging of colloidal systems out of equilibrium", PhD thesis (University of Crete, 2011).

[50] J. F. Brady, "The rheological behavior of concentrated colloidal dispersions", J. Chem. Phys. **99**, 567 (1993).

[51] J. F. Brady, "The long-time self-diffusivity in concentrated colloidal dispersions", J. Fluid Mech. **272**, 109 (1994).

[52] T. Ando and J. Skolnick, "Crowding and hydrodynamic interactions likely dominate in vivo macromolecular motion", Proc. Natl. Acad. Sci. U. S. A. **107**, 18457 (2010).

[53] R. Mari, R. Seto, J. F. Morris, and M. M. Denn, "Discontinuous shear thickening in brownian suspensions by dynamic simulation", Proc. Natl. Acad. Sci. U. S. A. **112**, 15326 (2015).

[54] A. Sierou and J. F. Brady, "Rheology and microstructure in concentrated noncolloidal suspensions", J. Rheol. **46**, 1031 (2002).

[55] S. Gallier, E. Lemaire, F. Peters, and L. Lobry, "Rheology of sheared suspensions of rough frictional particles", J. Fluid Mech. **757**, 514 (2014).

[56] M. Wang and J. F. Brady, "Spectral ewald acceleration of stokesian dynamics for polydisperse suspensions", J. Comput. Phys. **306**, 443 (2016).

[57] L. Durlofsky, J. F. Brady, and G. Bossis, "Dynamic simulation of hydrodynamically interacting particles", J. Fluid Mech. **180**, 21 (1987).

[58] D. Lindbo and A.-K. Tornberg, "Spectrally accurate fast summation for periodic Stokes potentials", J. Comput. Phys. **229**, 8994 (2010).

[59] D. Lindbo and A.-K. Tornberg, "Spectral accuracy in fast Ewald-based methods for particle simulations", J. Comput. Phys. **230**, 8744 (2011).

[60] A. J. Banchio and J. F. Brady, "Accelerated Stokesian Dynamics: brownian motion", J. Chem. Phys. **118**, 10323 (2003).

[61] X. Bian, S. Litvinov, M. Ellero, and N. J. Wagner, "Hydrodynamic shear thickening of particulate suspension under confinement", J. Non-Newtonian Fluid Mech. **213**, 39 (2014).

[62] T. Kawasaki, D. Coslovich, A. Ikeda, and L. Berthier, "Diverging viscosity and soft granular rheology in non-brownian suspensions", Phys. Rev. E **91**, 012203 (2015).

[63] D. J. Evans and G. Morriss, *Statistical mechanics of nonequilibrium liquids* (Cambridge University Press, 2008).

[64] M. Bouzid, M. Trulsson, P. Claudin, E. Clément, and B. Andreotti, "Nonlocal rheology of granular flows across yield conditions", Phys. Rev. Lett. **111**, 238301 (2013).

[65] A. S. Khair, M. Swaroop, and J. F. Brady, "A new resistance function for two rigid spheres in a uniform compressible low-reynolds-number flow", Phys. Fluids **18**, 043102 (2006).

[66] J. W. Swan and J. F. Brady, "Colloidal dispersions deformed by a steady shear stress", Submitted (2013).

[67] M. Trulsson, B. Andreotti, and P. Claudin, "Transition from the viscous to inertial regime in dense suspensions", Phys. Rev. Lett. **109**, 118305 (2012).

[68] E. DeGiuli, G. Düring, E. Lerner, and M. Wyart, "Unified theory of inertial granular flows and non-brownian suspensions", Phys. Rev. E **91**, 062206 (2015).

[69] E. Lerner, G. Düring, and M. Wyart, "A unified framework for non-brownian suspension flows and soft amorphous solids", Proc. Natl. Acad. Sci. U.S.A. **109**, 4798 (2012).

[70] Y. Forterre and O. Pouliquen, "Flows of dense granular media", Annu. Rev. Fluid Mech. **40**, 1 (2008).

[71] K. Kamrin and G. Koval, "Nonlocal constitutive relation for steady granular flow", Phys. Rev. Lett. **108**, 178301 (2012).

[72] M. Bouzid, A. Izzet, M. Trulsson, E. Clément, P. Claudin, and B. Andreotti, "Non-local rheology in dense granular flows. revisiting the concept of fluidity", Eur. Phys. J. E **38**, 125 (2015).

[73] J. H. Simpson and H. Y. Carr, "Diffusion and nuclear spin relaxation in water", Phys. Rev. **111**, 1201 (1958).

[74] I. Chang and H. Sillescu, "Heterogeneity at the glass transition: translational and rotational self-diffusion", J. Phys. Chem. B **101**, 8794 (1997).

[75] A. J. Banchio, G. Nägele, and J. Bergenholtz, "Viscoelasticity and generalized stokes-einstein relations of colloidal dispersions", J. Chem. Phys. **111**, 8721 (1999).

[76] A. J. Banchio, J. Bergenholtz, and G. Nägele, "Rheology and dynamics of colloidal suspensions", Phys. Rev. Lett. **82**, 1792 (1999).

[77] D. Bonn and W. K. Kegel, "Stokes-Einstein relations and the fluctuation-dissipation theorem in a supercooled colloidal fluid", J. Chem. Phys. **118**, 2005 (2003).

[78] T. G. Mason, K. Ganesan, J. H. van Zanten, D. Wirtz, and S. C. Kuo, "Particle tracking microrheology of complex fluids", Phys. Rev. Lett. **79**, 3282 (1997).

[79] T. M. Squires and T. G. Mason, "Fluid mechanics of microrheology", Annu. Rev. Fluid Mech. **42**, 413 (2010).

[80] M. D. Ediger, "Spatially heterogeneous dynamics in supercooled liquids", Annu. Rev. Phys. Chem. **51**, 99 (2000).

[81] S. Gupta, J. Stellbrink, E. Zaccarelli, C. N. Likos, M. Camargo, P. Holmqvist, J. Allgaier, L. Willner, and D. Richter, "Validity of the Stokes-Einstein Relation in Soft Colloids up to the Glass Transition", Physical Review Letters **115**, 128302 (2015).

[82] A. Ikeda and K. Miyazaki, "Glass transition of the monodisperse gaussian core model", Phys. Rev. Lett. **106**, 015701 (2011).

[83] A. Ikeda and K. Miyazaki, "Slow dynamics of the high density Gaussian core model", J. Chem. Phys. **135**, 054901 (2011).

[84] S. F. Edwards and R. B. S. Oakeshott, "Theory of powders", Physica A **157**, 1080 (1989).

[85] P. Sollich, F. Lequeux, P. Hebraud, and M. E. Cates, "Rheology of soft glassy materials", Phys. Rev. Lett. **78**, 2020 (1997).

[86] P. Hébraud and F. Lequeux, "Mode-coupling theory for the pasty rheology of soft glassy materials", Phys. Rev. Lett. **81**, 2934 (1998).

[87] J. S. Langer, "Shear-transformation-zone theory of viscosity, diffusion, and stretched exponential relaxation in amorphous solids", Phys. Rev. E **85**, 051507 (2012).

[88] M. L. Falk and J. S. Langer, "Deformation and failure of amorphous, solidlike materials", Annu. Rev. Condens. Matter Phys. **2**, 353 (2011).

[89] L. F. Cugliandolo, "The effective temperature", J. Phys. A: Math. Theor. **44**, 483001 (2011).

[90] I. K. Ono, D. J. O'Hern C. S.and Durian, S. A. Langer, A. J. Liu, and S. R. Nagel, "Effective Temperatures of a Driven System Near Jamming", Physical Review Letters **89**, 095703 (2002).

[91] H. A. Makse and J. Kurchan, "Testing the thermodynamic approach to granular matter with a numerical model of a decisive experiment", Nature **415**, 614 (2002).

[92] L. Berthier and J.-L. Barrat, "Shearing a Glassy Material: Numerical Tests of Nonequilibrium Mode-Coupling Approaches and Experimental Proposals", Phys. Rev. Lett. **89**, 095702 (2002).

[93] L. Berthier and J.-L. Barrat, "Nonequilibrium dynamics and fluctuation-dissipation relation in a sheared fluid", J. Chem. Phys. **116**, 6228 (2002).

[94] M. Zhang and G. Szamel, "Effective temperatures of a driven, strongly anisotropic brownian system", Phys. Rev. E **83**, 061407 (2011).

[95] T. K. Haxton, "Ratio of effective temperature to pressure controls the mobility of sheared hard spheres", Physical Review E **85**, 011503 (2012).

[96] C. Eisenmann, C. Kim, J. Mattsson, and D. A. Wetiz, "Shear melting of a colloidal glass", Phys. Rev. Lett. **104**, 035502 (2010).

[97] T. Sentjabrskaja, P. Chaudhuri, M. Hermes, W. C. K. Poon, J. Horbach, S. U. Egelhaaf, and M. Laurati, "Creep and flow of glasses: strain response linked to the spatial distribution of dynamical heterogeneities", Sci. Rep. **5**, 11884 (2015).

[98] R. Besseling, E. R. Weeks, A. B. Schofield, and W. C. K. Poon, "Three-Dimensional Imaging of Colloidal Glasses under Steady Shear", Phys. Rev. Lett. **99**, 028301 (2007).

[99] J. F. Brady, "Brownian motion, hydrodynamics, and the osmotic pressure", J. Chem. Phys. **98**, 3335 (1993).

[100] J. F. Brady, A. S. Khair, and M. Swaroop, "On the bulk viscosity of suspensions", J. Fluid Mech. **554**, 109 (2006).

[101] B. D. Lubachevsky and F. H. Stillinger, "Geometric properties of random disk packings", J. Stat. Phys. **60**, 561 (1990).

[102] M. Skoge, A. Donev, F. H. Stillinger, and S. Torquato, "Packing hyperspheres in high-dimensional Euclidean spaces", Phys. Rev. E **74**, 041127 (2006).

[103] D. M. Heyes and J. R. Melrose, "Brownian dynamics simulations of model hard-sphere suspensions", J. Non-Newtonian Fluid Mech. **46**, 1 (1993).

[104] M. Swaroop, "The bulk viscosity of suspensions", PhD thesis (California Institute of Technology, 2010).

[105] J. Bergenholtz, J. F. Brady, and M. Vivic, "The non-newtonian rheology of dilute colloidal suspensions", J. Fluid Mech. **456**, 239 (2002).

[106] G. K. Batchelor and J. T. Green, "The hydrodynamic interaction of two small freely-moving spheres in a linear flow field", J. Fluid Mech. **56**, 375 (1972).

[107] J. F. Brady and J. F. Morris, "Microstructure of strongly sheared suspensions and its impact on rheology and diffusion", J. Fluid Mech. **348**, 103 (1997).

[108] J. F. Brady and M. Vivic, "Normal ststress in colloidal dispersions", J. Rheol. **39**, 545 (1995).

[109] P.-E. Peyneau and J.-N. Roux, "Frictionless bead packs have macroscopic friction, but no dilatancy", Phys. Rev. E **78**, 011307 (2008).

[110] D. Bonn, J. Paredes, M. M. Denn, L. Berthier, T. Divoux, and S. Manneville, "Yield stress materials in soft condensed matter", arXiv:1502.05281 (2015).

[111] M. D. Rintoul and S. Torquato, "Metastability and crystallization in hard-sphere systems", Phys. Rev. Lett. **77**, 4198 (1996).

[112] A. Ikeda, L. Berthier, and P. Sollich, "Disentangling glass and jamming physics in the rheology of soft materials", Soft Matter **9**, 7669 (2013).

[113] W. Götze, *Complex dynamics of glass-forming liquids: a mode-coupling theory* (Oxford University Press, 2008).

[114] B. M. Guy, M. Hermes, and W. C. K. Poon, "Towards a unified description of the rheology of hard-particle suspensions", Phys. Rev. Lett. **115**, 088304 (2015).

[115] A. Fall, N. Huang, F. Bertrand, G. Ovarlez, and D. Bonn, "Shear thickening of cornstarch suspensions as a reentrant jamming transition", Phys. Rev. Lett. **100**, 018301 (2008).

[116] R. Seto, R. Mari, J. F. Morris, and M. M. Denn, "Discontinuous shear thickening of frfriction hard-sphere suspensions", Phys. Rev. Lett. **111**, 218301 (2013).

[117] J. R. Royer, D. L. Blair, and S. D. Hudson, "Rheological signature of frictional interactions in shear thickening suspensions", Phys. Rev. Lett. **116**, 188301 (2016).

[118] A. Ikeda, L. Berthier, and P. Sollich, "Comment on "constant stress and pressure rheology of colloidal suspensions"", Phys. Rev. Lett **116**, 179801 (2016).

[119] C. K. C. Lieou and J. S. Langer, "Nonequilibrium thermodynamics in sheared hard-sphere materials", Phys. Rev. E **85**, 061308 (2012).